Chemical Science

ROYAL SOCIETY OF CHEMISTRY

REVIEW

View Article Online
View Journal | View Issue

Cite this: *Chem. Sci.*, 2025, **16**, 17058

Formulating cathode materials based on high-entropy strategies for sodium-ion batteries

Zhuozheng Hong,[abc] Zhuang-Chun Jian, [ac] Yan-Fang Zhu,*[ac] Yan-Jiang Li,[ace] Qi-Cong Ling,[ac] Hanshen Xin, *[d] Didi Wang,[b] Chao Wu*[b] and Yao Xiao *[ac]

Sodium-ion batteries (SIBs) are promising alternatives to lithium-ion batteries (LIBs) owing to abundant resources and cost-effectiveness. However, cathode materials face persistent challenges in structural stability, ion kinetics, and cycle life. This review highlights the transformative potential of high-entropy (HE) strategies that leveraging multi-principal element synergies to address these limitations *via* entropy-driven mechanisms. By establishing thermodynamic criteria for high-entropy materials (HEMs), we elucidate the universal principles whereby configurational entropy mitigates lattice distortion, suppresses phase transitions, and enhances Na^+ diffusion kinetics *via* multi-element interactions. HE design demonstrates unique advantages for layered oxides, Prussian blue analogues (PBAs) and polyanionic cathode systems: it alleviates Jahn–Teller distortion through dopant synergy to stabilize layered structures; optimises ion migration channels by tuning exposed crystal facets; suppresses irreversible phase changes and mechanical strain to enable reversible structural evolution; and enhances redox reversibility *via* multi-site charge compensation among transition metals. Furthermore, reasonable design principles for the HE strategy in cathode materials for SIBs were proposed, along with the future expansion of theoretical calculations and the application of the HE strategy in the future. At the same time, potential challenges that may occur during this process and the current viewpoints and methods for solving these problems were emphasized. Overall, this review provides valuable guidance for the further exploration of the HE strategy in the field of SIBs.

Received 15th July 2025
Accepted 21st August 2025

DOI: 10.1039/d5sc05245a

rsc.li/chemical-science

1 Introduction

Under the rapid development of global current energy vehicles and the expanding demand for energy storage, the production scale of lithium-ion batteries (LIBs) has increased significantly.[1–6] In the future, the supply of lithium resources is expected to fall far short of the demand generated by new energy vehicles and power infrastructure, exacerbating the lithium shortage and having a negative impact on global carbon neutrality efforts in the medium to long term.[7–11] Given this lithium scarcity, the abundant global reserves of sodium have led to an increasing research interest in replacing LIBs with sodium-ion batteries (SIBs) (Fig. 1a).[12–19] SIBs exhibit superior performance in low-temperature conditions, over-discharge resistance, safety, and environmental protection, positioning them as a promising alternative to LIBs with broad application prospects.[20,21] In recent years, the high-entropy (HE) approach has emerged as an innovative concept in materials science and has been widely applied in various domains, including catalysis,[22–25] electrochemical energy storage,[26–36] environmental protection,[37,38] and thermoelectrics.[39] Currently, the high-entropy materials (HEMs) consisted of multiple distinct elements within a single phase have been explored in various fields. The interactions among these elements exhibit superior performance in materials science, enabling solutions to numerous practical challenges.[40–42]

Elemental doping usually refers to the incorporation of a small amount of secondary elements into the main material, which is an effective way to endow SIB materials with good performance.[43,44] However, this simple elemental doping method has certain limitations in terms of exploration and performance optimization. To significantly expand the available composition space and unlock new research directions, the HE approach has emerged as a research hotspot in cathode design for SIBs, as evidenced by the keyword clustering analysis in Fig. 1b. The HE approach combines multiple principal elements at equiatomic or near-equiatomic ratios. Unlike conventional

[a]*College of Chemistry and Materials Engineering, Wenzhou University, Wenzhou, Zhejiang 325035, P. R. China. E-mail: xiaoyao@wzu.edu.cn; yanfangzhu@wzu.edu.cn*
[b]*Institute of Energy Materials Science (IEMS), University of Shanghai for Science and Technology, Shanghai, 200093, P. R. China. E-mail: chaowu@usst.edu.cn*
[c]*Zhejiang Provincial Key Laboratory of Advanced Battery Materials and Technology, Wenzhou University Technology Innovation Institute for Carbon Neutralization, Wenzhou, Zhejiang 325035, China*
[d]*School of Microelectronics, Shanghai University, Shanghai, 201800, P. R. China. E-mail: xinhanshen@shu.edu.cn*
[e]*Key Laboratory of Spin Electron and Nanomaterials of Anhui Higher Education Institutes, Suzhou University, Suzhou 234000, China*

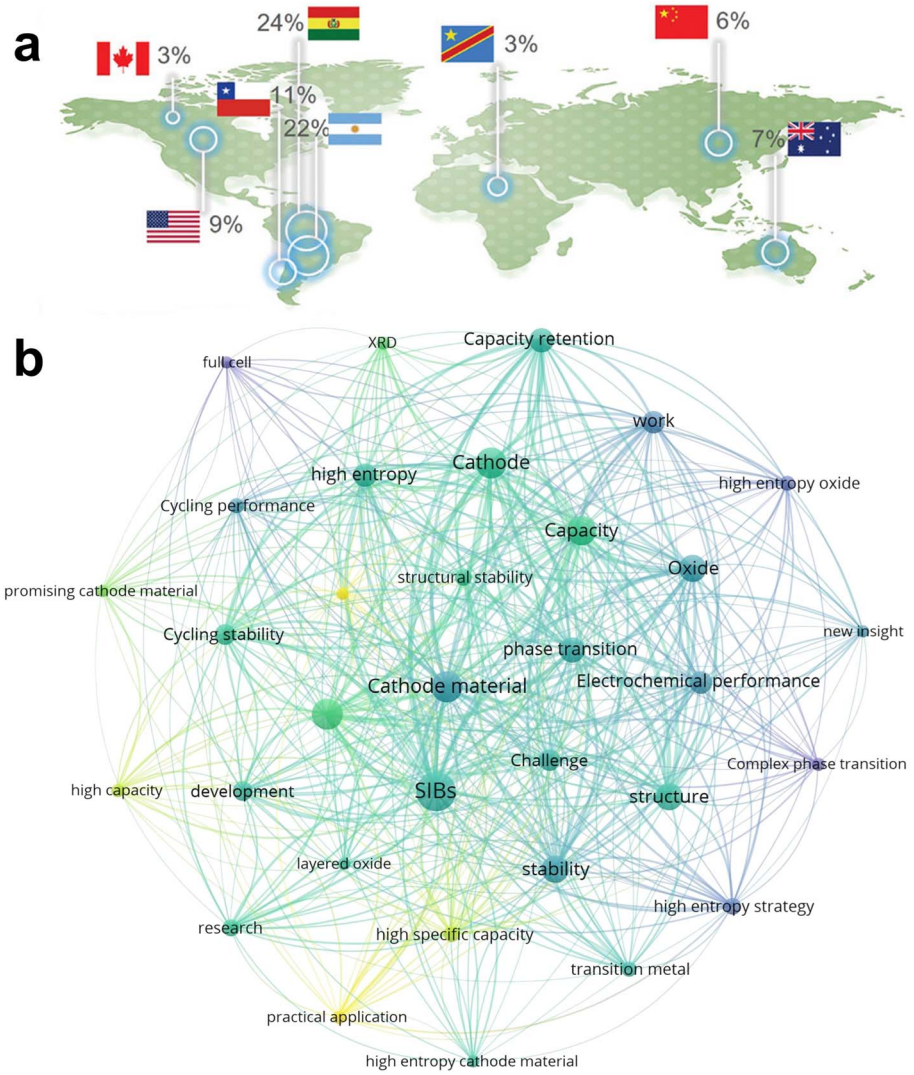

Fig. 1 (a) Distribution of global lithium resources. Reprinted with permission from ref. 2. Copyright 2024 John Wiley and Sons. (b) Research hotspots in the HE cathode of SIBs.

doping, this strategy enhances compositional flexibility in compositional and structural design, resulting in a wider range of crystal and electronic structures. In addition, the incorporation of multiple elements can cause local disorder within the lattice, thereby increasing the system's disorder and enhancing its tolerance to structural evolution during electrochemical processes. At the same time, specific defects may be introduced, which optimize ion migration channels and indirectly facilitate electron migration by modulating the electronic structure.[45]

The growing interest in this strategy is further quantified by the sharp rise in both publications and citations of HE-based SIB cathodes over recent years.[46] The cathode materials utilized in SIBs can be categorized into three primary groups: layered oxides,[47–49] polyanionic,[50–52] and Prussian blue analogues (PBAs).[53–55] Layered oxide materials exhibit high energy density, excellent rate performance, and structural diversity. However, their practical applications are impeded by their susceptibility to atmospheric moisture and rapid capacity degradation. Polyanionic cathodes show remarkable stability and superior long-cycle performance. Nevertheless, they are subject to inherent limitations such as poor electrical conductivity and the need for material modification using carbon coating, doping, *etc.* These constraints pose significant challenges and will result in reduced energy density. PBA emerges as a promising sodium storage material owing to its distinctive metal–organic framework structure, which presents exceptional energy density. Nevertheless, for existing Prussian blue materials, removing crystalline water presents a substantial challenge, which dramatically determines their electrochemical performances. HEMs show remarkable advantages compared to traditional materials. The HE effect boosts the compatibility among elements, allowing for the formation of stable single-phase solid solutions at relatively lower temperatures.[56] The differences in atomic radius and electronegativity of multiple elements will cause local fluctuation in lattice potential energy. This mainly inhibits the continuous diffusion of transition

metal (TM) atoms through vacancies, thus reducing their ability for disordered migration.[57,58] Such a particular effect not only helps maintain the structural stability but also restrains atomic migration phenomena that could potentially undermine the cycle stability during the battery cycling process. Simultaneously, the HE structure can more effectively address the changes in local interaction forces brought about by the Na^+ intercalation/deintercalation and the redox reactions of TM elements. Due to this adaptability, HEMs can effectively prevent irreversible phase transitions during charging and discharging, significantly enhancing the structural stability and long-cycle performance. The rapid development of these different cathode materials highlights the transformative potential of HE engineering in the development of high-performance SIBs. Therefore, given the broad design prospects offered by HE strategies, the development of high-performance HEMs is undoubtedly within reach. Fig. 2 summarizes the landmark research achievements in chronological order, demonstrating the rapid development of HE strategies in the cathodes for SIB.[59,60]

In 2020, Zhao *et al.* officially incorporated the HE concept into the design of SIBs. They synthesized the layered oxide cathode materials that contained as many as nine TM elements. Compared with traditional doped materials, these newly developed materials demonstrated outstanding long-term cycling stability. Specifically, after 500 cycles, their capacity retention could reach up to 83%. These materials also showed highly reversible O3–P3 phase transformation characteristics. Notably, more than 60% of the total capacity was stored in the layered O3 region. Additionally, the research team put forward the mechanism of the HE structure. These findings laid the foundation for the development of HE and further advanced the application of the HE strategy in SIBs.[61] Although the HE strategy presents numerous possibilities for SIB materials, current research in this area remains in its nascent stage, and the fundamental concept of HEMs lacks precision.[62–67] Initially, it was believed that when there were more than five metallic elements, the material was considered a HEM. Later, configurational entropy was introduced to determine whether it was a HEM, but this method could only be applied to some materials. This is the severe challenge faced by the implementing of the HE strategy in battery materials. Therefore, it is imperative to deeply investigate the working mechanism of multi-component structures in battery materials, provide a clear definition of HE, and elucidate various action mechanisms of different HEMs. In this review, we provide an overview of the most recent studies on the application of HEMs in various components of SIBs. We emphatically examine its influences on the phase structures and electrochemical characteristics of electrode materials, and propose to integrate the HE strategy

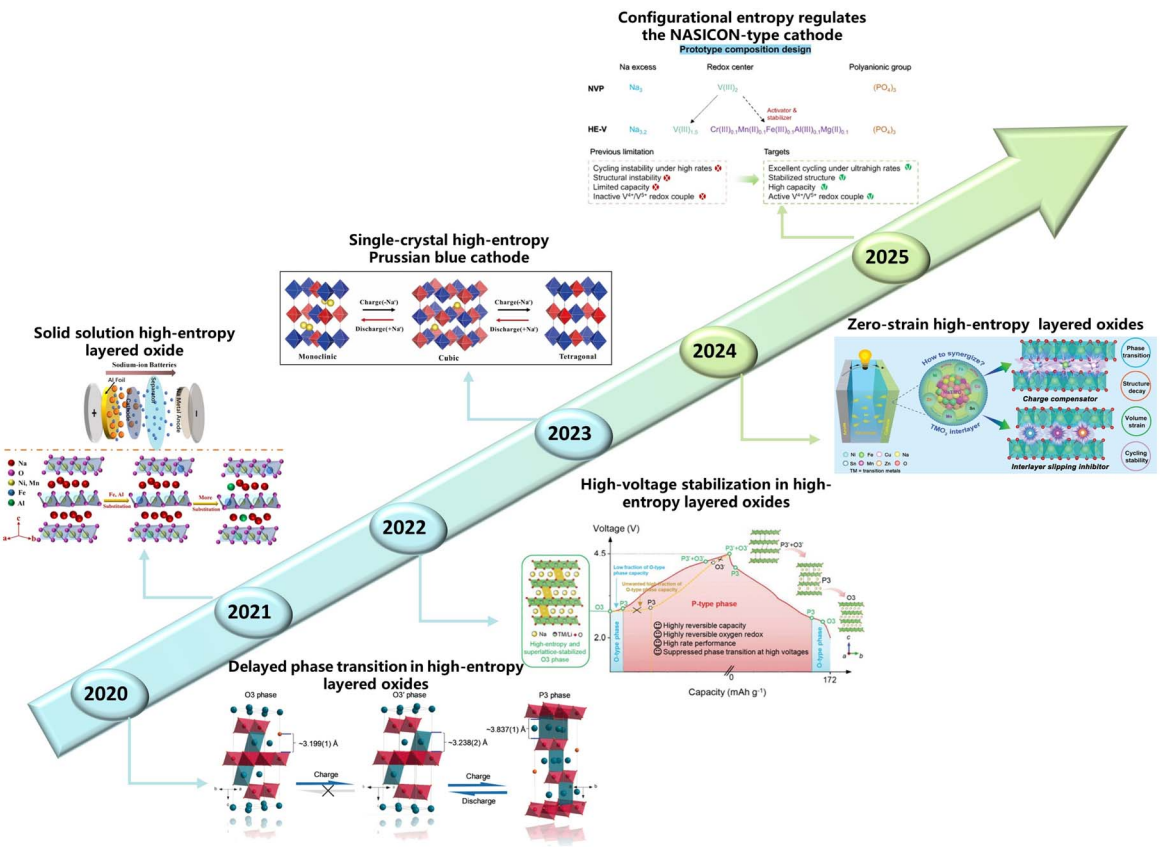

Fig. 2 Timeline of representative works on HEMs for sodium-ion batteries. All the illustrations are from the literature. Reprinted with permission from ref. 92. Copyright 2020 Wiley VCH. Reprinted with permission from ref. 59. Copyright 2021 Springer Nature. Reprinted with permission from ref. 107. Copyright 2022 John Wiley and Sons. Reprinted with permission from ref. 121. Copyright 2023 Elsevier. Reprinted with permission from ref. 115. Copyright 2024 Wiley VCH. Reprinted with permission from ref. 60. Copyright 2025 RSC.

into the overall design principles of battery materials as well as the future development direction.

2 Definition and mechanism of HEMs

2.1 The basic concept of entropy

The design of HEMs mainly comes from the rational use of entropy.[68] First, we need to understand the role of entropy in the system. Based on the second law of thermodynamics, within an isolated system where no energy transfer occurs between the system and its surroundings the system inherently evolves in a direction that increases randomness, which always increases the entropy of the entire system and is known as the entropy increase principle ($\Delta S \geq 0$).[69] The second law of thermodynamics can also be applied to non-isolated systems when considering their surroundings. At constant temperature and pressure, the change in Gibbs free energy (ΔG) of the system must be less than or equal to zero (≤ 0). For processes at equilibrium, the ΔG remains unchanged, while for spontaneous processes, ΔG decreases.[70] A non-isolated system will transition from its initial condition to an end state characterized by the lowest G value.[71] Therefore, according to both criteria, S determines whether the process is in equilibrium.

2.2 Process and definition of HE

In 2004, the principle of HE within materials was first proposed.[72] Yeh *et al.* described the properties of high entropy alloys (HEAs), which consist of five or more principal elements, where the atomic proportion of each component falling between 5% and 35%.[73–75] Subsequently, the principle of HE was applied to a wide range of battery materials, including cathode,[76,77] anode and electrolyte materials in SIBs.[78,79] What these materials have in common is that they incorporate five or more metallic elements into the same lattice position. However, this definition of HEMs remains too broad to specifically distinguish between low-entropy and medium-entropy materials.[80]

To evaluate the different mixing entropies, the configurational entropy change (ΔS_{config}) of the compositions are generally used according to the following formula:

$$S_{\text{config}} = -k \ln w \tag{1}$$

$$S_{\text{config}} = -R\left[\left(\sum_{i=1}^{N} x_i \ln x_i\right)_{\text{cation-site}} + \left(\sum_{j=1}^{N} x_j \ln x_j\right)_{\text{anion-site}}\right] \tag{2}$$

$$S_{\text{config}} = R \ln N \tag{3}$$

$$\Delta G_{\text{mix}} = \Delta H_{\text{mix}} - T\Delta S_{\text{mix}} \tag{4}$$

In this context, k represents the Boltzmann constant (1.38×10^{-23} J K^{-1}),[81] w denotes the degeneracy factor, R is the molar gas constant [8.314 J (mol^{-1} K^{-1})], N signifies the number of components, x_i represents the molar fraction of cations, and x_j indicates the molar fraction of anions.[82] ΔH_{mix} represents the mixing enthalpy, ΔS_{mix} refers to the mixing entropy, and T denotes the absolute temperature. For single-phase HEMs where the ΔS_{config} is greater than or equal to 1.5 R, the product of temperature and mixing entropy ($T\Delta S_{\text{mix}}$) exceeds the ΔH_{mix}. Therefore, the overall Gibbs free energy change (ΔG_{mix}) becomes negative, achieving entropy-stabilized conditions (Fig. 3a and b). Materials exhibiting a ΔS_{config} of 1.5 R or greater are classified as HE systems. Those with a ΔS_{config} between 1 R and 1.5 R (including 1 R but excluding 1.5 R) are categorized as medium-entropy, and materials with a ΔS_{config} less than 1 R are designated as low-entropy systems.[83] Elements of varying sizes can induce the formation of disordered structures, leading to an atomic size mismatch effect. Consequently, certain materials, despite fulfilling the criteria for HEAs, exhibit inherent instability, with some displaying multiple phase states.[84] It is important to note that the definition of HEAs and their derivatives remains an evolving area of research. Currently, a majority of research focuses on boosting ΔS_{config} by incorporating multiple elements, aiming to explore the structural

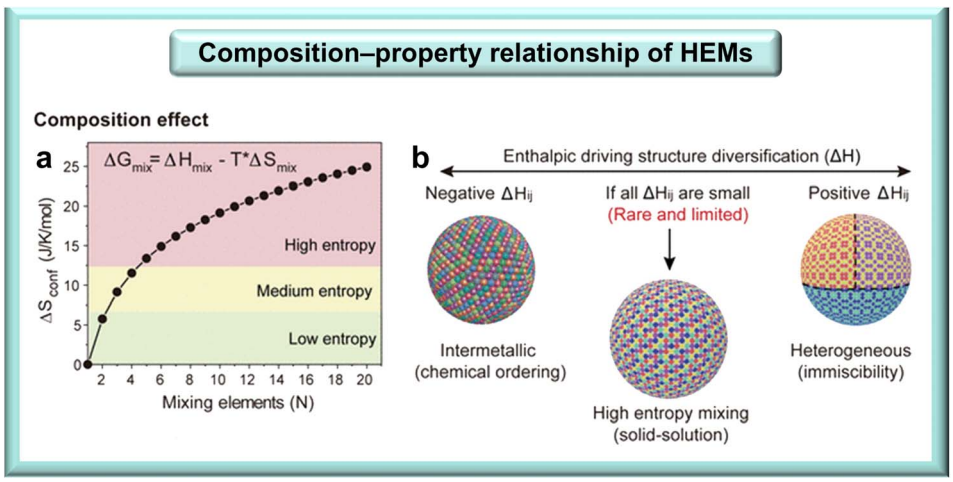

Fig. 3 Thermodynamic analyses of the HE mixing considering both (a) entropy and (b) enthalpy, which are mainly determined by the composition of the HEMs. Reprinted with permission from ref. 83. Copyright 2024 Elsevier.

stability and enhanced properties of materials attributed to the HE effect.[85,86]

The calculation of ΔS_{config} is further extended to include oxides with multiple cation sites,[87] such as perovskite oxides ABO_3, where A and B represent cations occupying 12- and 6-coordination sites, respectively.[88,89]

$$S_{config} = -R\left[\left(\sum_{i=1}^{M} x_a \ln x_a\right)_{A\ \text{cation-site}} + \left(\sum_{i=1}^{L} x_b \ln x_b\right)_{B\ \text{cation-site}} + \left(\sum_{i=1}^{N} x_j \ln x_j\right)_{\text{anion-site}}\right] \quad (5)$$

where x_a, x_b, and x_j represent the mole fractions of the elements at the A, B, and anion sites, respectively, while M, L, and N denote the number of cations at the A, B, and anion sites, correspondingly.[90] These precise definitions establish well-defined boundaries for classifying HE materials. However, this definition has significant limitations when applying the thermodynamic concept of entropy to emerging fields such as liquid electrolytes and certain negative electrode materials, or when determining the ΔS_{config} values of specific materials like battery materials.

2.3 Four core effects of HE

HE effect. The ΔS_{config} within the material increases, which reduces the free energy of the solid solution phases. This, in turn, promotes the development of these structures. In most HE materials, while ΔS_{config} does contribute to their formation and stability, when compared with enthalpy, it is not always the determining factor. Additionally, other factors like intrinsic defects also have a substantial impact on influencing stability.

Lattice distortion effect. When several elements simultaneously occupy the same (sub)lattice position, geometric distortion is bound to occur. The extent of this distortion is determined by factors such as the size, valence state, and electronegativity of the atoms or ions co-existing within the same (sub)lattice. Excessive distortion may lead to structural collapse, which in turn affects the performance of the material. Conversely, it has been demonstrated that appropriate lattice distortion can alter the energy landscape of the ion diffusion pathway.[91] This then creates a percolation network that facilitates ion migration.

Sluggish diffusion effect. Compared to conventional materials, the ion diffusion kinetics and associated phase transitions in HE bulk materials are significantly slowed due to the increased migration barriers arising from atomic size mismatch and local lattice distortions. In HE bulk materials, multiple ions are usually incorporated into TM sites and do not participate in the de-intercalation/intercalation process. The differences between adjacent atoms in crystal sites can increase the migration barrier among these sites, thereby reducing the unnecessary movement of metal ions.[92] This suppression of migration may also hinder the phase transition, as this process requires the coordinated diffusion of many elements and the uniform sliding of TM layers.

Cocktail effect. During the mixing process, the synergistic effects among different components can lead to the formation of HEMs, and their performance is likely to be improved. This improvement cannot be merely attributed to the characteristics of any single component. Instead, it stems from the complex interactions among numerous components. Even minor alterations in the types and ratios of elements can cause significant changes in the functionality of the system. Therefore, in practical applications, the performance of materials can be adjusted (Fig. 4).[93,94]

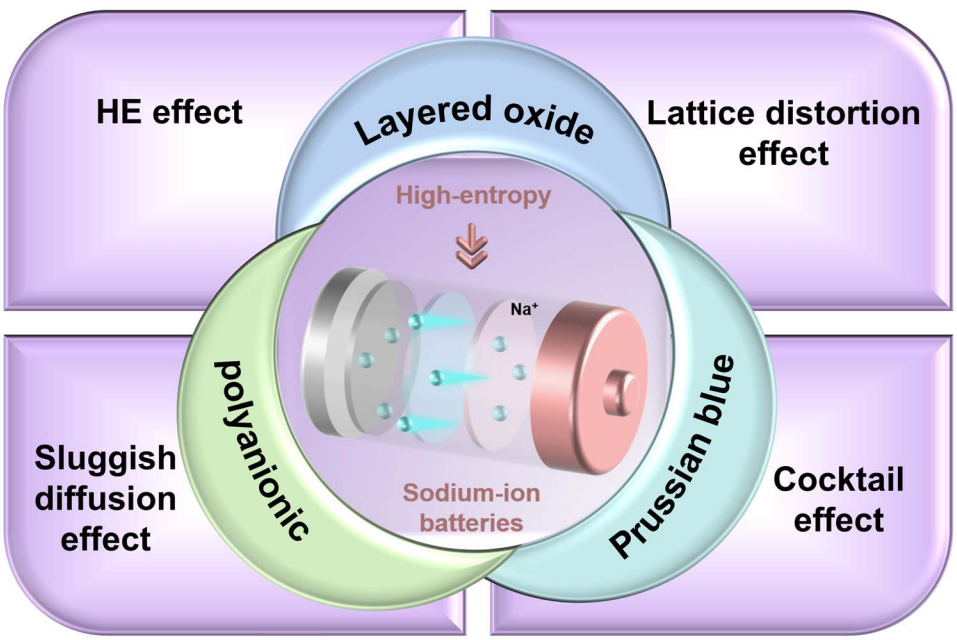

Fig. 4 The following diagram provides an overview of the four core effects of HE that are employed in SIB cathodes.

3 HE cathode materials

Since excellent electrochemical performance has been achieved by introducing the HE strategy into cathode materials for SIBs, HE cathodes have gained increasing attention. Based on the categories of cathodes, there are three types of HE cathodes: layered oxides, PBAs, and polyanionic. All of them exhibit better performance as expected when HE strategy is applied to these materials. In the case of oxide cathodes, high-entropy oxides (HEOs) can provide higher reversible capacity and exhibit smoother voltage profiles due to their superior structural stability and a special charge compensation mechanism involving multiple elements. In 2021, Ma *et al.* first proposed HEPBAs, in which five elements (iron, manganese, nickel, copper and cobalt) occupy one lattice position. HEPBA materials have more Na^+ transport sites and lower vacancy concentration, making the framework structure more stable and thus avoiding battery failure caused by structural collapse. In addition, the significant reduction in crystalline water content after HE modification also enhances its long-cycle stability.[95] In the field of polyanionic compound cathodes, Wu *et al.* designed a HE polyanion material by substituting multiple elements at the V site *in situ*. The obtained material has more aggregated particles, which can inhibit crystal growth. Further, it can shorten the migration path of Na^+ in the solution under the HE effect, and accelerate the migration kinetics of Na^+. In conclusion, the HE strategy plays a key role in improving the electrochemical performance of the cathode in SIBs. Understanding and in-depth exploration of the functional mechanism of HEA cathodes are crucial for providing novel and effective ideas for the design of high-performance cathode materials for SIBs.

The rational design and preparation of HE cathode materials are pivotal for the advancement of practical applications. However, the intricate compositional complexity poses challenges in synthesis, such as reducing particle size and enhancing uniform mixing. In fact, it is the homogeneous blending of diverse elements that leads to substantial variations in chemical and physical properties, such as melting points and electrochemical behavior. Therefore, a precise approach to design and prepare HE cathodes can improve both the structure and battery performance.[96,97]

3.1 HE layered oxide cathodes

Currently, several key factors limit the performance of the layered oxide cathode. Upon cycling, irreversible phase transitions, as well as TM and/or O ions transfer, result in performance degradation.[98,99] Simultaneously, volume expansion during cycling leads to rapid decay in battery capacity and shortens the cycle life. Furthermore, due to structural instability, cation migration and irreversible lattice oxygen loss contribute to voltage attenuation and poor kinetics.[100–105] Benefiting from the unique properties of HEAs, compared with common oxide cathodes, HEOs cathodes possess a larger layer distance in the TM layers and a more stable structure. In 2019, Hu *et al.* pioneered the application of HE principles to O3-type oxide cathode materials. Through *in situ* X-ray powder diffraction (XRD) analysis, they highlighted that HE played a role in stabilizing intricate phase transitions within these oxides. They

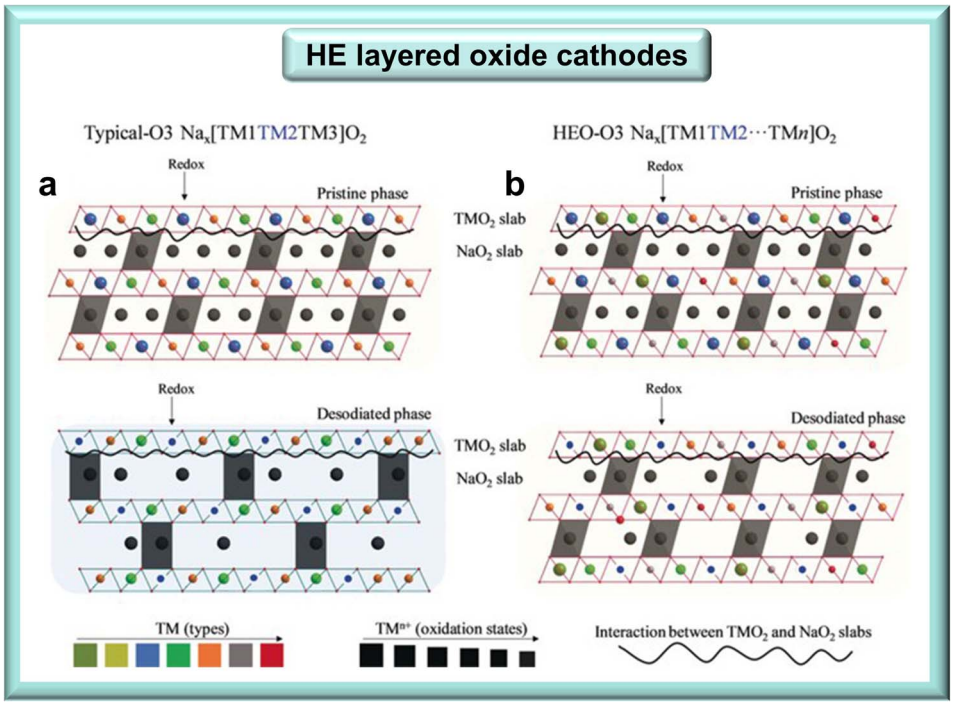

Fig. 5 (a) The conventional O3-type Na-based layered oxides contain three different TM elements. (b) The proposed HEO cathodes have multiple TM elements (TM_2 represents the redox elements and is marked in blue). Reprinted with permission from ref. 92. Copyright 2020 Wiley VCH.

demonstrated that multi-element doping broadened the layer spacing of TM layers and accelerated Na^+ migration, and then improved stability and rate performance (Fig. 5a and b). Therefore, the HE approach offers novel and significant ideas for developing high-performance oxide cathode materials.

Layered oxides are regarded as one of the most promising cathode materials for SIBs due to their high energy density and straightforward synthesis process. However, when redox reactions occur at TM sites, the lattice stress caused by volume changes will weaken the bonding force between TMs and oxygen. Under high-voltage conditions, oxygen release is prone to occur, resulting in irreversible structural alterations during cycling. Additionally, TM dissolution and lattice cracking during cycling also affect the stability of the oxide cathode. Considering the benefits of HEAs, researchers have developed HEOs by modifying the ratio and type of TMs. These materials demonstrate excellent structural stability, enhanced fracture toughness, superior performance at both high and low temperatures, and outstanding electrochemical properties.

3.1.1 Mitigating Jahn–Teller distortion. To investigate the significance of HE strategies in enhancing structural evolution. Cheng *et al.* designed $Na_{0.7}Mn_{0.4}Ni_{0.3}Cu_{0.1}Fe_{0.1}Ti_{0.1}O_{1.95}F_{0.1}$ by using $Na_xMn_{1-y}M_yO_2$ as a substrate for HE doping. This boosted the initial Coulomb efficiency and structural integrity.

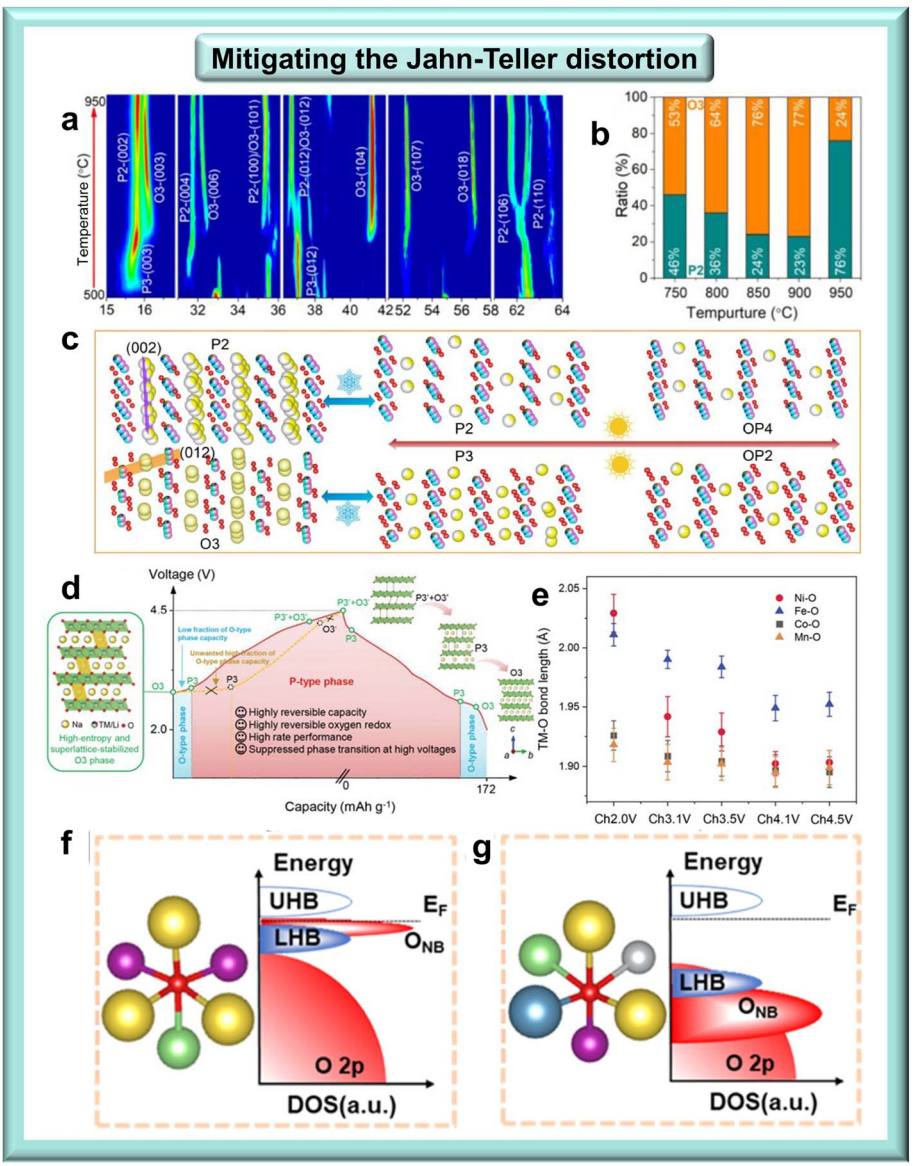

Fig. 6 HE affects structural transformation. (a) XRD of $Na_{0.7}Mn_{0.4}Ni_{0.3}Cu_{0.1}Fe_{0.1}Ti_{0.1}O_{1.95}F_{0.1}$ at different temperatures during calcination. (b) The ratios of P2/O3 phases in NaMnNiCuFeTiOF sintered at various temperatures. (c) Schematic illustration of the structural change mechanisms of $Na_{0.7}Mn_{0.4}Ni_{0.3}Cu_{0.1}Fe_{0.1}Ti_{0.1}O_{1.95}F_{0.1}$. Reprinted with permission from ref. 106. Copyright 2023, Elsevier. (d) Schematic diagram of the charging and discharging behavior of $Na_{2/3}Li_{1/6}Fe_{1/6}Co_{1/6}Ni_{1/6}Mn_{1/3}O_2$. (e) The bond length changes of TM–O (where TM represented Ni, Fe, Co, and Mn) varies during the charging process from 2.0 to 4.5 V. Reprinted with permission from ref. 107. Copyright 2022 John Wiley and Sons. Schematic diagram of the DOS for (f) LMM and (g) LMCNM. Reprinted with permission from ref. 108. Copyright 2025 American Chemical Society.

Moreover, adjusting the sintering temperature allowed for controlling over the proportion of the P2/O3 phase as shown in Fig. 6a and b.[106] High-angle annular dark field (HAADF) and X-ray photoelectron spectroscopy (XPS) analyses were carried out to explore the function of HE doping elements. The results showed that the Ni not only provided charge compensation but also exhibited reversible migration to Na layers under high pressure, playing a good role as a structural support. The reversible Ni^{2+}/Ni^{3+}, Mn^{3+}/Mn^{4+}, and Fe^{3+}/Fe^{4+} ions served for charge compensation, whereas Ti and Cu were non-active elements during charging and discharging, facilitating the development of a sodium-free vacancy-ordered P2/O3 composite structure. HE doping significantly mitigated the Jahn–Teller distortion of Mn^{3+} and established robust TM–F bonds. This not only effectively restrained the slippage of the TM layer during the Na^+ intercalation but also contributed to the structural stability. The combined influence of multiple elements facilitated the formation of a stable P2/O3 composite structure across a broad temperature range in HE cathodes (Fig. 6c).

Yao *et al.* successfully prepared $Na_{2/3}Li_{1/6}Fe_{1/6}Co_{1/6}Ni_{1/6}Mn_{1/3}O_2$ HE cathodes, achieving an ultra-stable superlattice structure with Li/TM ordering (Fig. 6d).[107] X-ray absorption spectroscopy (XAS) analysis showed that the redox of $Ni^{2+}/Ni^{3+}/Ni^{4+}$ and Fe^{3+}/Fe^{4+} provided a high coulombic efficiency during charge/discharge processes. The Mn^{4+} and Co^{3+} significantly improved the stability of the material during Na^+ ion intercalation, suppressing Jahn–Teller distortion. Most importantly, the superlattice structure remained intact after long-term charge/discharge cycles. The reversible substitution between Li^+ and Na^+ and their interactions with different TMs dramatically enhanced the diffusion kinetics of Na^+, stabilized the material's structure, and significantly reduced the irreversible phase transition. Extended X-ray absorption fine structure (EXAFS) analysis presented that in the TM–O coordination shell layer of the material, the atomic spacing at the K-edge of Ni and Fe was markedly shortened due to the oxidation of Ni and Fe, while the changes in Co and Mn were less pronounced. The K-edge transformation of Ni, Co, Fe, and Mn resulted from the reversible O3/P3 phase transition in the low-voltage region of the superlattice structure. The small deviation in the Fourier transform of the TM–O and TM–TM shell layers during the initial charge transfer more clearly indicated the stability of this superlattice structure with multiple element interactions (Fig. 6e). Generally speaking, by applying this HE strategy, it was possible to realize a rapid and reversible O3–P3 phase transition in the low-voltage range. Moreover, in the high-voltage region, the phase transition and oxygen redox reaction can be effectively suppressed. As a result, even under the conditions of high cut-off charging voltage and high cycling rate, high reversible capacity and outstanding stability could be achieved. The integration of HE and superlattice stabilization provided more opportunities for regulating the structure and phase transition, as well as the reversibility and activity of oxygen redox reactions *via* Li–TM interactions in layered cathode materials.

Due to the wide availability of P2-type Mn-based layered oxide, they are expected to be widely employed in large-scale electrochemical energy storage. However, the trivalent manganese in the MnO_6 octahedron has a tendency to experience significant phase transformation and lattice oxygen loss at high working voltages. This issue severely impairs the capacity and cycling stability of these materials. Li *et al.* putted forward a ΔS_{config} tuning approach to optimize the P2-type $Na_{0.8}Li_{0.17}Mg_{0.18}Mn_{0.66}O_2$ (LMM) cathode. The synthesized cathode material, $Na_{0.8}Li_{0.17}Ca_{0.025}Mg_{0.12}Ni_{0.05}Mn_{0.66}O_2$ (LMCNM), adhered to the standard $P6_3/mmc$ crystal phase. Notably, this material demonstrated a capacity retention of 92% after 100 cycles at a 0.4C rate (where 1C is defined as 125 mA h g^{-1}). Moreover, during charge–discharge cycles at a relatively high working voltage range of 2.0–4.3 V, it showed a minimal volume change of only 0.94%. *In situ* XRD, *ex situ* XPS, and computational analysis together suggested that there was no obvious Jahn–Teller distortion upon cycling for LMCNM (as shown in Fig. 6f and g). Instead, there was clear evidence of charge compensation from Mn^{3+} to Mn^{4+}. Additionally, by co-doping with Ca and Ni, partial reversible anionic redox was achieved, which helped to balance the requirements of stability and high capacity.

Due to the Jahn–Teller effect of high-spin Mn^{3+} and Ni^{3+}, Ni and/or Mn are dominant in layered oxides, which leads to structural distortion and electrode instability. Increasing ΔS_{config} through HE strategies can significantly enhance the disorder of the system, uniformly disperse local stress, and effectively suppress the stretching of bond lengths of elements such as Mn^{3+}, thereby improving the Jahn–Teller effect. This design not only improves the lifespan and rate performance of the cathode materials, but also provides a new idea for the development of high-energy-density and high-safety SIBs.

3.1.2 Facilitating ion transport kinetics. The HEOs can facilitate the exposure of more (010) active crystalline surfaces by modulating the surface energy, constructing more channels for Na^+ migration. Hu *et al.* constructed a HE configuration in the TMO_2 layers of $NaNi_{0.4}Fe_{0.2}Mn_{0.4}O_2$ (NFM424), resulting in the formation of a HE $NaNi_{0.25}Mg_{0.05}Cu_{0.1}Fe_{0.2}Mn_{0.2}Ti_{0.1}Sn_{0.1}O_2$ (HEP424).[109] The ellipsoidal shape of HEP424 could be attributed to the elevated ΔS_{config} found in the TMO_2 layers, which promoted selective growth of specific crystal planes, thereby influencing the final material's structure. Specifically, the enhanced growth rates of the (100), (010), and (003) crystal planes improved Na^+ transport kinetics (Fig. 7a and b). Gradual doping with additional elements leaded to an increase in ΔS_{config} and caused the particles to evolve into larger ellipsoidal shapes. The HE structure notably elevated the surface energy of the (003) plane, which promoted the exposure of the (010) active crystal facet and consequently improved the electrochemical performance. Additionally, the enlarged TMO_2 layers greatly mitigated Jahn–Teller distortion at the Ni^{3+} active center (Fig. 7c).

Fu *et al.* used $Na_{0.62}Mn_{0.67}Ni_{0.37}O_2$ as a base for multi-element doping to design the HEM $Na_{0.62}Mn_{0.67}Ni_{0.23}Cu_{0.05}Mg_{0.07}Ti_{0.01}O_2$ (CuMgTi-571). Besides structural stability, such HE material with abundant active crystal surfaces provided rapid Na^+ transport.[110,111] The CuMgTi-571 microparticles exhibited a hexagonal single-crystal structure. The active crystal

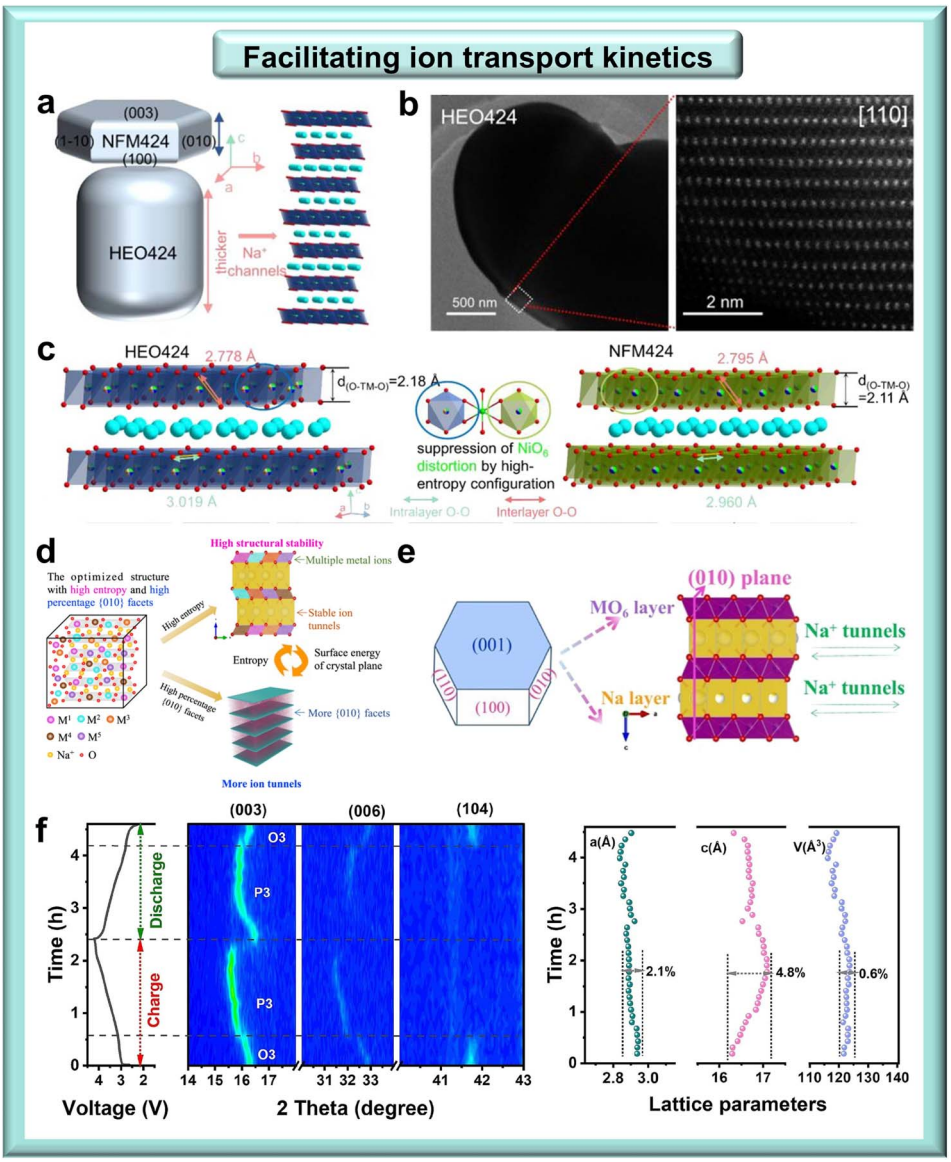

Fig. 7 Some effects of HE on the crystal surface. (a) Schematic diagram of the morphological structure of the HEM compared with the normal material. (b) HAADF-STEM images of HEO424. (c) The HEM possesses a variety of cations that provide highly stable structures and diffusion channels, making more (010) active crystalline surfaces for ion transport. Reprinted with permission from ref. 109. Copyright 2022 American Chemical Society. (d) The six (010) active crystalline planes of HEM. (e) Variation of (010) active crystalline facet content with the change of ΔS_{config}. Reprinted with permission from ref. 111. Copyright 2022 Springer Nature. (f) *In situ* XRD patterns and corresponding lattice parameter changes of TMO5. Reprinted with permission from ref. 112. Copyright 2025 Elsevier.

planes displayed an open atomic arrangement structure (Fig. 7d), which was more favorable for Na^+ transfer. As illustrated in Fig. 7e, by examining various materials with differing entropy values, it was observed that the proportion of active crystalline planes was improved as the increase of ΔS_{config}. Furthermore, for materials with straightforward compositions and lower entropy, their surface energy is predominantly affected by temperature. In contrast, the surface energy of complex multicomponent systems with higher entropy is chiefly influenced by ΔS_{config}. Therefore, the aforementioned P2 materials were mainly ruled by ΔS_{config}, which modulated the growth rates of various crystallographic facets, resulting in high-performance HEO cathodes.

O3-type layered oxides are regarded as promising cathode materials for SIBs because of their high theoretical capacity. However, they frequently encounter issues such as structural instability and poor Na^+ diffusion, which result in rapid capacity fading. Wang *et al.* proposed a HE strategy combined with a synergistic multi-metal effect to address these limitations. This was accomplished by improving the structural stability and reaction kinetics. A novel O3-type layered HE cathode material, $Na_{0.9}Fe_{0.258}Co_{0.129}Ni_{0.258}Mn_{0.258}Ti_{0.097}O_2$ (TMO5),[112] was synthesized *via* a simple solid-state method. The integration of experimental analysis and *in situ*/non-*in situ* characterizations verified that the HE metal ion mixture is advantageous for enhancing the reversibility of redox reactions and the O3–P3–

O3 phase transition process (Fig. 7f), as well as increasing the Na^+ diffusion rate. Due to its structural and compositional advantages, TMO5 presented a higher initial specific capacity of 159.6 mA h g^{-1}. After 100 cycles at 2C, it still exibited a specific capacity of 110.1 mA h g^{-1}, with a capacity retention rate as high as 85.6%. This study indicated that HE design is a promising approach to develop robust and high-performance O3-type layered oxide cathodes as well.

The HE strategy introduces multiple metal elements in nearly equimolar ratios to form layered oxide materials. The unique HE effect significantly promotes the Na^+ transfer kinetics from multiple aspects. The random distribution of multiple principal elements causes significant local lattice distortions. Such distortions are not disordered but form a rich variety of local microenvironments with different energies within the framework of the average crystal structure. This complex local environment can soften the energy barriers along the Na^+ diffusion paths. Some local sites may form depressions with lower energy or wider bottlenecks, providing more low-energy migration paths or lower migration activation energy for Na^+, thereby accelerating the two-dimensional diffusion of Na^+ between TM layers.

3.1.3 Suppressing phase transition. It is well known that the relatively large ionic radius of Na^+ inevitably leads to ordered sodium vacancies in the crystal lattice of layered oxides. During the charging and discharging processes, the sliding of the TM layer generally result in complex structural evolutions. Therefore, these materials are prone to occur irreversible phase transitions.[113,114] Using multi-element doping to increase ΔS_{config} and then suppress irreversible phase transitions as well as improve Na^+ transport kinetics is becoming one of the valid way to enhance the electrochemical performance of layered cathode materials.

As reported by Hu *et al.*, the TM sites in the HE cathode material $NaNi_{0.12}Cu_{0.12}Mg_{0.12}Fe_{0.15}Co_{0.15}Mn_{0.1}Ti_{0.1}Sn_{0.1}Sb_{0.04}O_2$ were occupied by nine different TM ions, resulting in an unexpectedly super-stable structure and exhibiting excellent cycling stability and high sodium storage capacity. Such HE cathode presented a capacity retention of 83% after 500 cycles and approximately 80% at 5C. Upon cycling, the material underwent a highly reversible O3 to P3 phase transformation, with more than 60% of its total capacity residing in the O3-type structure. The phase transition behavior of the samples was illustrated in Fig. 8a. In comparison with traditional O3-type layered oxide, the TM elements within the multi-component HEO cathode exhibited obvious interaction characteristics, which leaded to more distinct local interactions between Na in NaO_2 and the elements in the TM layer during the charging and discharging process. Seven TM elements participated in charge compensation, resulting in intricate variations in their oxidation states. Concurrently, the sodium content adjusted accordingly due to Na^+ intercalation and deintercalation processes, inducing structural localization and phase transitions (Fig. 8b).[92] For conventional O3 phase cathodes, the elements involved in redox reactions are generally uniformly distributed in the lattice to minimize energy. As their ionic size and oxidation state change, the phase transitions of the overall material structure were easily visualized. However, for HEMs with multiple elements acting together, the HE composition leads to a stochastic distribution of the redox elements. Local fluctuations were accommodated by an increased diversity of local structural characteristics, effectively delaying the phase transition.

The work reported by Molenda *et al.* developed a HE $NaMn_{0.2}Fe_{0.2}Co_{0.2}Ni_{0.2}Ti_{0.2}O_2$, which featured a dual-phase structure comprising O3(1) and O3(2) phases (Fig. 8c).[115] As shown in Fig. 8d, the structural development exhibited a highly reversible phase transitions, characterized by the conversion process from O3 to P3 and returned to O3. With the assistance of HE doping, the P3 phase was able to be maintained in high voltage states. The precise phase composition of $NaMn_{0.2}Fe_{0.2}Co_{0.2}Ni_{0.2}Ti_{0.2}O_2$ during desodiation and sodiation was illustrated in Fig. 8e. The highly reversible O3–P3 phase transition mitigated the impact of oxygen vacancies, resulting in this ultrastable HEM cathode.

Wang *et al.* have created a new six-component HEO O3–$Na(Fe_{0.2}Co_{0.2}Ni_{0.2}Ti_{0.2}Sn_{0.1}Li_{0.1})O_2$.[116] This material enabled highly reversible electrochemical reactions and phase transitions. After 100 cycles at a current density of 0.5C, such HEO cathode could still maintain 81% of its initial capacity, proving outstanding stability. Moreover, it also demonstrated outstanding rate performance. This phenomenon was ascribed to a relatively high Na^+ diffusion coefficient, which was greater than 5.75×10^{-11} cm^2 s^{-1}, outperforming many previously reported O3-type cathodes. In addition, the HE cathode manifested excellent compatibility with the hard carbon anode, achieving a specific capacity of 90.4 mA h g^{-1} (with an energy density of 267 Wh kg^{-1}). *In situ* XRD and XAS of iron revealed that charge compensation was facilitated by redox reactions involving Ni^{2+}/Ni^{3+}, Co^{3+}/Co^{4+}, and Fe^{3+}/Fe^{2+} pairs. The disordered arrangement of multi-component TMs in the HEO restricted the ordering of charge and sodium vacancies. Consequently, the interlayer slipping and phase transitions were prevented.

The random distribution of the material results in the formation of a highly disordered TM layer, which in turn destroys the long-range order of the lattice. This, in turn, serves to reduce the driving force of phase transition and thereby inhibit the phase transition caused by Na^+ deposition fundamentally. Concurrently, the disparity in atomic size and chemical properties, the local stress caused by the release of dispersed Na^+ will also inhibit the structural instability. This design not only solves the problem of cycle stability of the layered oxide cathode but also provides a new way for developing high-voltage and high-capacity SIBs. Further studies are required to achieve the collaborative optimization of phase transition inhibition and ion dynamics by entropy regulating in the future.

3.1.4 Regulating lattice strain. A large number of O3 layered oxide cathode materials suffer from inherent thermal and chemical–mechanical instability, which can lead to lattice cracking due to lattice oxygen escape and lattice stress. Fortunately, the multi-element interactions in HE doping greatly reduce lattice defects and cracks caused by structural strain. Cui

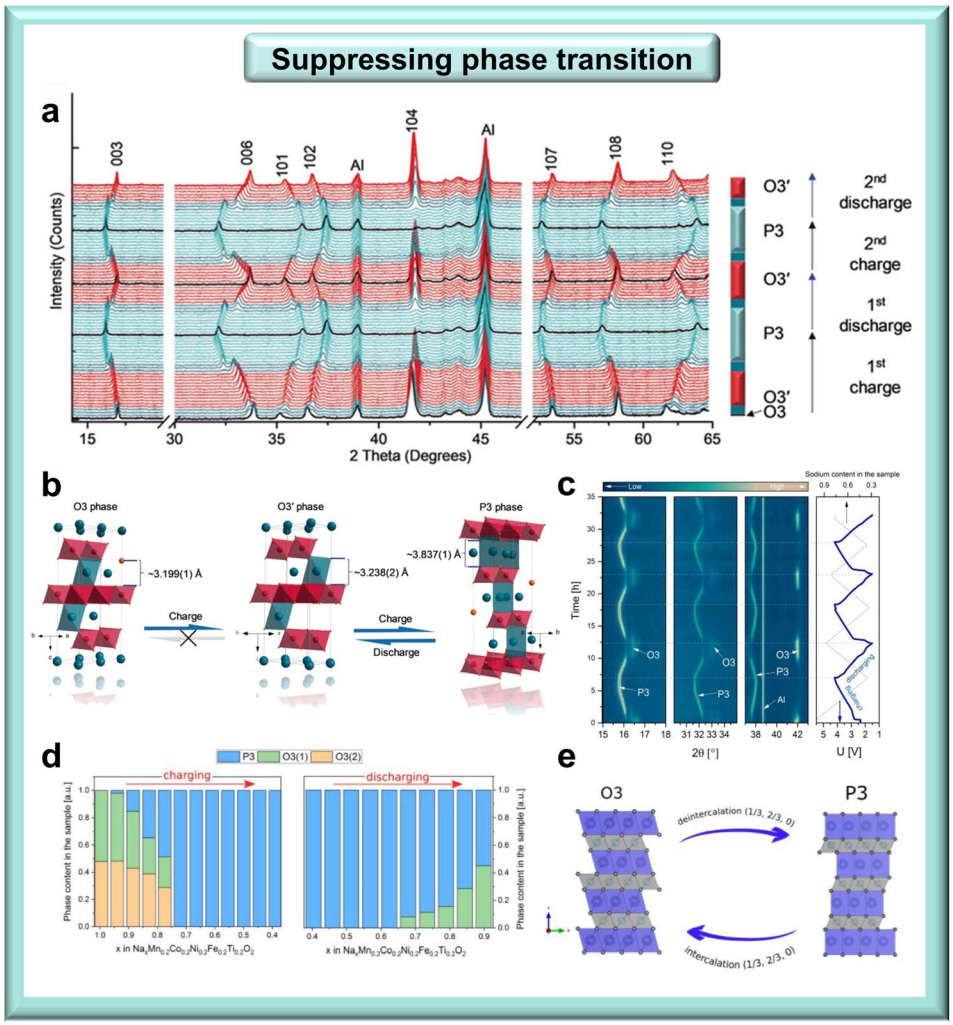

Fig. 8 Suppression of phase transition through HE design. (a) *In situ* XRD patterns of $NaNi_{0.12}Cu_{0.12}Mg_{0.12}Fe_{0.15}Co_{0.15}Mn_{0.1}Ti_{0.1}Sn_{0.1}Sb_{0.04}O_2$ within 2.0–3.9 V at 0.1C. (b) Crystal structure evolution of the HE layered oxide cathode. Reprinted with permission from ref. 92. Copyright 2020 Wiley VCH. (c) *In situ* XRD patterns of $NaMn_{0.2}Fe_{0.2}Co_{0.2}Ni_{0.2}Ti_{0.2}O_2$ during charge/discharge cycling. (d) Variations in the content of O3 and P2 phases during the first charge/discharge cycle. (e) Graphical visualization of O3- and P3-type crystal structures. Reprinted with permission from ref. 115. Copyright 2022 Elsevier.

et al. reported a HE cathode composed of $NaNi_{0.2}Fe_{0.2}Mn_{0.35}Cu_{0.05}Zn_{0.1}Sn_{0.1}O_2$ for SIBs, which enabled highly reversible phase evolution and zero volume strain (Fig. 9a), significantly enhancing the cycling performance of the entire battery system.[117] Fig. 9b illustrated that the electron cloud density surrounding Sn/Mn/Zn atoms was relatively high, indicating a strong charge localization around these elements, which reinforced the coordination of oxygen and Sn/Mn/Zn in the TM layer, thereby inhibiting slipping within the TMO_2 slab during Na^+ intercalation/deintercalation processes. Consequently, the pinning effect exerted by Sn/Mn/Zn elements contributed to the remarkable reversibility observed in phase transitions of HEMs. Furthermore, the formation energy and ΔS_{config} during sodium removal (Fig. 9c and d) indicated that with the removal of Na, the absolute value of material formation energy gradually decreased, suggesting a diminishing contribution to structural stability over time. Conversely, along with an increase in ΔS_{config} due to TM disordering, Na^+ withdrawal further enhanced the system's ΔS_{config} by establishing a disordered environment composed of Na^+ and vacancies. This effectively compensated for structural instability arising from reduced formation energy (notably, contrasting changes occur during discharge). Thus, the thermodynamic benefits derived from HE effects within crystal structures emerged as another critical factor underpinning reversible phase transitions in HEMs. This research provided comprehensive insights into how the synergistic interactions among multiple elemental functionalities could be harnessed to develop advanced cathode materials for sustainable SIBs.

Xiao *et al.* incorporated eight TM elements into the same lattice site of O3–$NaNi_{0.5}Mn_{0.5}O_2$ (NMMO) and designed a HEO cathode material $NaNi_{0.1}Mn_{0.15}Co_{0.2}Cu_{0.1}Fe_{0.1}Li_{0.1}Ti_{0.15}Sn_{0.1}O_2$, achieving ultra-strong mechanical properties at the microscale.[110] The integrity of the crystal structure could be maintained even after long cycling. After 50, 100, and 200 cycles, the cross-sections of NMMO and HEO particles were shown in Fig. 9e. Obviously, cracks were gradually formed and there were

a large number of dispersed cracks from the outside to the inside of the particles. Compared with NMMO, the surface morphology of HEO remained almost unchanged after cycling. The cracks penetrating the particles destroy the integrity of the cathode structure, leading to a series of side reactions and causing the TM ion migration and dissolution. Meanwhile, Young's modulus nanoindentation tests were conducted on HEO and NMMO to evaluate the structural damage during the

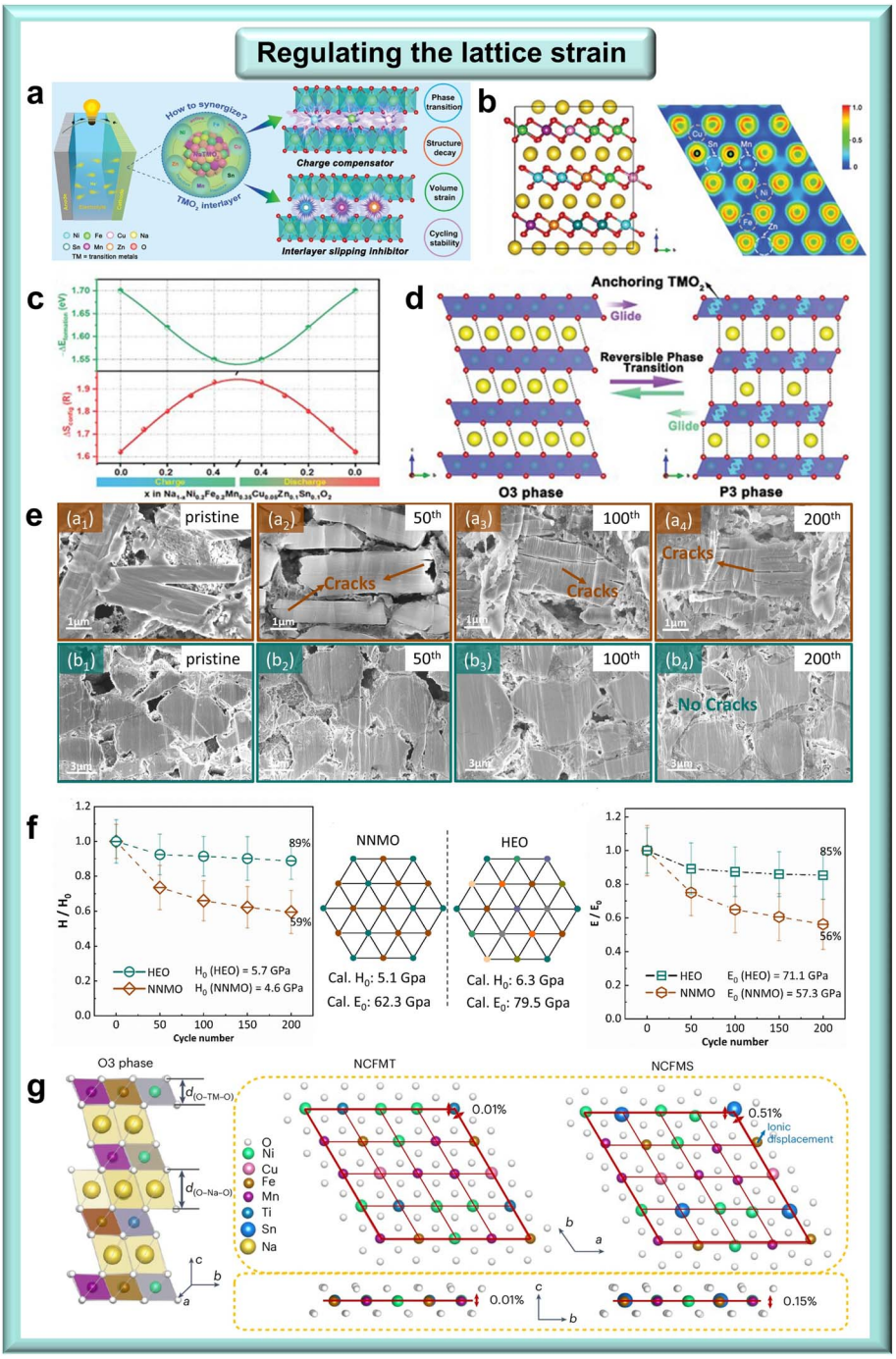

Fig. 9 Inhibition of grain surface strain by HE. (a) Schematic diagram of designing HE O3-type layer cathode material. (b) Crystal structure optimization diagram of HE cathode materials, showing the (001) crystal facet andELF. (c) The curves of Na^+ ion formation energy and ΔS_{config} during extraction and intercalation in HEMs. (d) Schematic diagram of reversible phase transition of O3-type HE cathode materials. Reprinted with permission from ref. 117. Copyright 2024 Wiley VCH. (e) SEM images of HEO and NMO before and after 200 cycles. (f) Calculation of hardness and Young's modulus for both materials. Reprinted with permission from ref. 110. Copyright 2023 Wiley VCH. (g) Structural model of O3 phase and schematic representation of the correlation between strain distribution and ionic displacement for NCFMT and NCFMS viewed in perpendicular and parallel to the TMO_2 layers. Reprinted with permission from ref. 118. Copyright 2024 Springer Nature.

cycling process. As seen, the Young's modulus of the pristine HEO was significantly greater than that of the NMMO (Fig. 9f).

Ding *et al.* synthesized O3-type HE $NaNi_{0.3}Cu_{0.1}Fe_{0.2}Mn_{0.3}Ti_{0.1}O_2$ (NCFMT) and $NaNi_{0.3}Cu_{0.1}Fe_{0.2}Mn_{0.3}Sn_{0.1}O_2$ (NCFMS) by substituting Ti^{4+} with Sn^{4+}.[118] The research found that NCFMT exhibited excellent coulombic efficiency and outstanding cycling stability, while NCFMS performed poorly because of structural instability. It has been revealed that the structural integrity of layered cathode materials is influenced by the compatibility of elements in the TM oxide layer. The planar strain in NCFMS was caused by metal ion displacement, leading to element separation and crack formation during cycling. In contrast, NCFMT demonstrated a stable structural framework due to the high mechanical-chemical compatibility among its constituent elements, which was conducive to the stable Na^+ storage (Fig. 9g).

Upon cycling, the repeated intercalation and deintercalation of Na^+ can cause significant lattice strain (volume change and lattice parameter fluctuation). This strain accumulation leads to microcracks in particles, an increased irreversibility of phase transitions, and thus seriously impairs cycle stability and rate performance. The HE strategy achieved fine control of lattice strain at the atomic and lattice scales. The core mechanism is reflected in the following aspects: (1) during deep desodiation process, the instability of oxygen ions (oxygen evolution) and the resulting TM migration and structural collapse cause significant lattice strain and capacity decay. The synergistic effect of multiple TMs can adjust the overall band structure and the position of the oxygen p-band center, enhancing the stability of oxygen. Strong lattice distortion and powerful inter-element interaction can anchor oxygen ions, inhibiting their migration and precipitation. (2) During the redox reactions triggered by Na^+ intercalation and deintercalation, the variations in bond lengths corresponding to different elements (such as the Jahn–Teller effect of Mn^{3+} and the significant volume contraction of Ni^{2+}/Ni^{4+}) show differences or even counteract each other at the local scale. This cocktail effect produced by the synergy of multiple elements effectively buffers the drastic volume fluctuation in local regions, disperses and minimizes the overall lattice strain, as well as prominently reduces the local lattice stress concentration. (3) The synergistic interactions among multiple elements enhance the mechanical stability of the lattice by distributing local stress uniformly, thereby preventing microcrack formation and improving long-term cycling performance.

3.1.5 Promoting charge compensation. The charge compensation mechanisms of different elements are crucial for the electrochemical properties of the products, which provides an important reference for investigating the role of various elements in the system and exploring the electrochemical reaction mechanisms in HEMs. The *ex situ* XAS spectra were used to analyze the redox state of the TMs in $NaMn_{0.2}Fe_{0.2}Co_{0.2}Ni_{0.2}Ti_{0.2}O_2$. For this HEM, the Mn presented +2, +3, and +4 oxidation states. In PFY mode, the peak on the right was considerably more prominent than the one on the left, suggesting a greater oxidation of Mn^{3+} to Mn^{4+}. The Mn spectrum revealed a significant oxidation of Mn during charging, whereas Mn underwent valence reduction during discharging.[115] The above observations showed that the reaction involved little Mn^{2+} and was mostly dominated by the redox of Mn^{3+}/Mn^{4+}. For Fe, the XAS spectra displayed that the material contained Fe^{3+}, and at first, only Fe^{3+} was visible in TEY and PFY modes. With the delocalization of Na^+, it shifted to higher energies, indicating the oxidation of Fe^{3+} (Fig. 10a and b). It could be concluded that Fe was not electrochemically active at the beginning, and the oxidation of Fe^{3+} only commenced following the phase transition from O3 to P3. Spectral analysis of Ni and Co showed that Co^{2+} and Co^{3+} ions appeared on the surface and in the lattice simultaneously before charging and discharging. The XAS characteristic peak become particularly sharp during the reaction, indicating that the entire oxidation reaction occurred rapidly. At the end of discharge, it was observed that a part of Co^{3+} was reduced to Co^{2+}. For Ni, it started at +2 valence, and during charging, Ni^{2+} was oxidized to a mixed +2/+3/+4 oxidation states. This high coulombic efficiency was ascribed to the synergistic effect among the Mn, Fe, Co, Ni, and Ti, while the charge compensation was originated from Mn and Ni species.

Wang *et al.* performed charge compensation analysis on O3–$Na(Fe_{0.2}Co_{0.2}Ni_{0.2}Ti_{0.2}Sn_{0.1}Li_{0.1})O_2$ HEMs.[116] The XAS analysis showed that Ti and Sn were non-electrochemically active elements, and the redox potentials of Ti^{3+}/Ti^{4+} and Sn^{4+}/Sn^{5+} were lower than 2 V. The XANES spectra of Fe, Co, and Ni at various charge/discharge states were analyzed. During the initial charging process, the K-edge of Ni shifts toward higher energies, suggesting that Ni was oxidized to a higher oxidation state. Since the K-edge energy of Ni at 4.1 V was higher than that of Ni^{3+}, it could be inferred that it was oxidized to approximately +3.5 at 4.1 V, providing a total capacity of about 72 mA h g^{-1}. Additionally, Fe and Co also experienced shifts to higher energy and were oxidized to approximately +3.5, both contributing partial capacity. During the first discharge, $Ni^{3.5+}$, $Co^{3.5+}$, and $Fe^{3.5+}$ were reduced. The K-edges of all three elements returned to lower absorption energies. After discharge to 3 V, the Ni K-edge continued to move toward lower energy levels, while Co and Fe showed no significant changes. This case indicated that the reduction of the Ni, Fe, and Co provided charge compensation in the voltage range of 4.1–3 V. From 3 V to 2 V, the Fe or Co was not involved in the redox reaction, while Ni was continuously reduced to +2 valence to provide charge compensation. They further analyzed the charge compensation mechanism of Fe by using Mössbauer spectroscopy. After charging to 4.1 V, an asymmetric double peak before charging revealed partial oxidation of Fe^{3+} to Fe^{4+}. It was further shown that Fe^{3+} in the HEO material exhibited electrochemical activity based on Fe^{3+}/Fe^{4+} redox couple. The spectra after complete discharge showed that there was no prominent high-spin Fe^{4+} in the HEO electrode. However, there were still noticeable differences from the original spectra, indicating that the structure of Fe was not completely restored after the first complete cycle, possibly due to a small amount of Fe^{4+} was not fully reduced to Fe^{3+} after the first cycle, and also that the HEO underwent slight structural distortion during the first cycle. In summary, the redox processes involved $Ni^{2+}/Ni^{3.5+}$, $Co^{3+}/Co^{3.5+}$, and some Fe^{3+}/Fe^{4+}

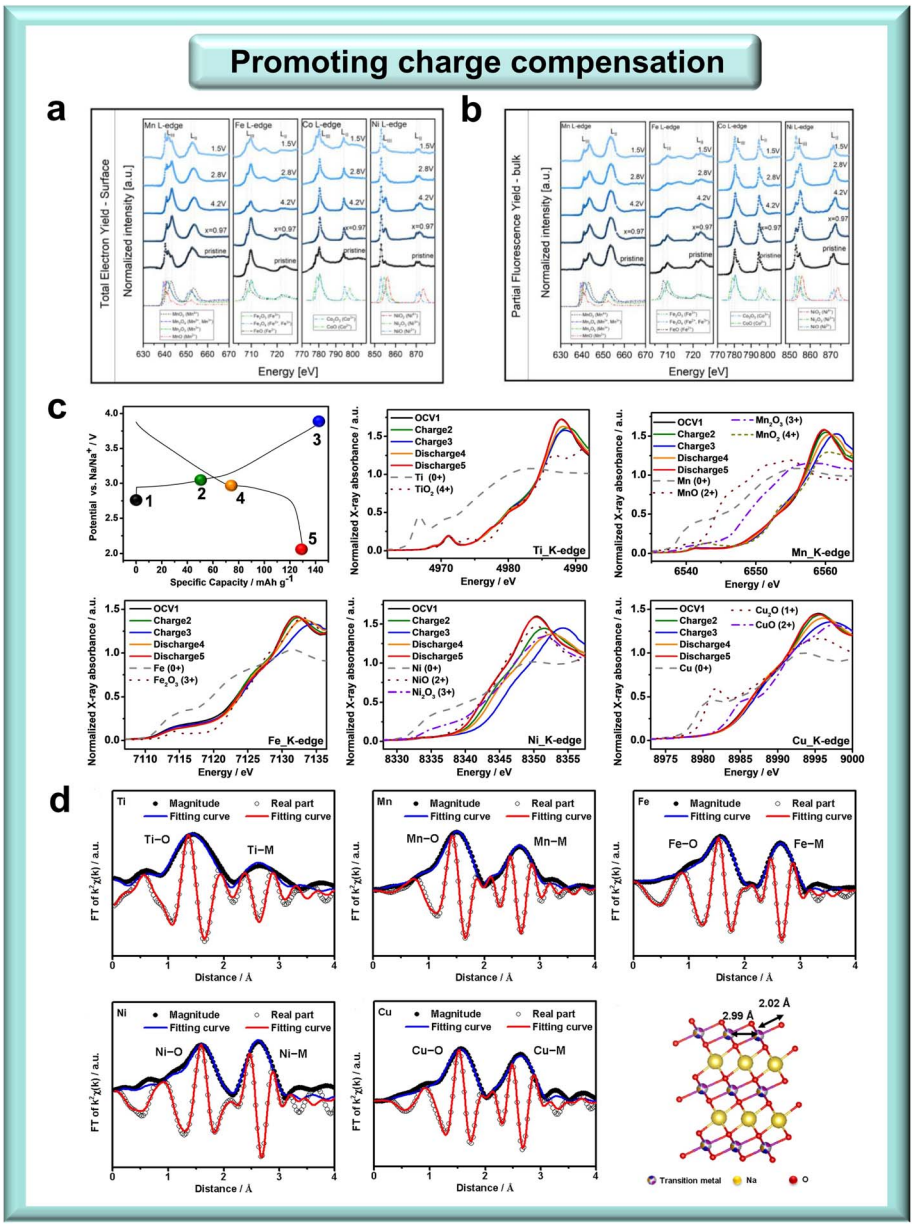

Fig. 10 *Ex situ* XAS spectra of TMs in $NaMn_{0.2}Fe_{0.2}Co_{0.2}Ni_{0.2}Ti_{0.2}O_2$ in both TEY (a) and PFY (b) modes during charging and discharging. Reprinted with permission from ref. 115. Copyright 2022 Wiley VCH. (c) Normalized *in situ* XANES spectra and the corresponding voltage curve of the NCNFMT at Ti, Mn, Fe, Ni, and Cu K-edges in various states. (d) K-edge XANES spectra of Ti, Mn, Fe, Ni, and Cu and the layered structure scheme where M–O and M–M bond lengths were optimized in NCNFMT. Reprinted with permission from ref. 119. Copyright 2022 Wiley VCH.

redox processes were crucial for charge balance, enabling this HEO's high reversible capacity.

Chen *et al.* designed a multi-element HE O3 cathode $NaCu_{0.1}Ni_{0.3}Fe_{0.2}Mn_{0.2}Ti_{0.2}O_2$. The charge compensation mechanism involving the Cu, Ni, Fe, Mn, and Ti K edges had be examined through XAS analysis as shown in Fig. 10c.[119] The HE electrodes in different states were known for their oxidation states of doping precursors such as Ti(IV)O_2, Mn(IV)O_2, Fe(III)$_2O_3$, Ni(II)O, and Cu(II)O. During the initial charge/discharge cycle, no notable shift in absorption was observed in the Ti and Mn spectra. However, a subtle change in intensity was still detectable, suggesting that there was a slight alteration in the chemical environment surrounding Ti and Mn, but the valence state remained unchanged. This was due to the increase in structural disorder around Mn caused by lattice distortion of Na^+ deinsertion and insertion, which also reflected the important role of entropy in stabilizing the structure. For the K-edge spectra of Fe and Cu, there was a small edge shift to higher energy during charging, but it reverted to the position of the original edge as discharge proceeded. Thus, the Fe^{3+}/Fe^{4+} and Cu^{2+}/Cu^{3+} were reversible redox couples, calculations indicated that the Fe and Cu occured redox reactions exclusively in the high-voltage range. For Ni's K-edge spectrum, the edge energy during the charged state exceeded that of Fe_2O_3. This behavior suggested the occurrence of Ni^{2+}/Ni^{4+} redox coupling, where the average oxidation state of Ni attained +4 upon full charging (Fig. 10d).

The above observations suggested that among the inactive elements in the stable structure, Fe and Cu contributed less to the capacity while Ni supplied more. The excellent performances of HEMs were attributed to the mutiple element symbiotic effect.

Liu *et al.* prepared the P2–$Na_{0.67}Mn_{0.6}Cu_{0.08}Ni_{0.09}Fe_{0.18}Ti_{0.05}O_2$ (MCNFT) cathode material, which exhibited enhanced stability in a deeply desodiated state.[113] This improvement facilitated internal Na^+ migration, thereby enhancing both charge capacity and coulombic efficiency. The novel MCNFT demonstrated promising results by extracting 0.61 Na and exhibiting superior reversibility compared to NMO. External XAS and XPS analyses showed that the charge capacity improved from 92.8 mA h g^{-1} to 158.1 mA h g^{-1} upon charging to 4.5 V, while the coulombic efficiency increased from 57.7% to 98.2%. These enhancements could be attributed to the synergistic effects of cationic and anionic redox reactions. Furthermore, *in situ* XRD analysis proved that the crystal structure maintained its stability even when subjected to high sodium removal conditions. These experimental observations were supported by density functional theory (DFT) calculations.

Due to the disordered TM distribution and the regulation of the electronic structure, uniform charge compensation is achieved. The multi-element electronegativity difference and orbital hybridization can reduce the charge compensation barrier energy, thereby comprehensively improving the efficiency, reversibility, and capacity of charge compensation. Future studies can further explore the redox matching of element combinations and the microscopic mechanism of anion/cation co-compensation. Therefore, the research progress of HE layered oxides was discussed in detail and their main components and electrochemical properties were summarized in Table 1.

3.2 HE Prussian blue cathodes

In 2021, researchers introduced five different metallic elements into the nitrogen coordination sites and successfully designed, for the first time, a HE Prussian blue material that exhibited a zero-strain reaction with excellent multiplicative properties and cyclic performance. It was worth mentioning that the crystalline water content of the HE material was significantly diminished, further enhancing its capacity, which greatfully promoted the development of Prussian blue cathode materials.[120–122]

Ma *et al.* designed a high-entropy HE-PBA featuring outstanding performance and a strain-free structure by incorporating five cations—Fe, Mn, Ni, Cu, and Co—at the nitrogen-coordinated M site. This material exhibited a ΔS_{config} value of 1.61 R as shown in Fig. 11a and b.[95] They performed the first *in situ* probing of the gas production behavior of HE-PBA using differential electrochemical mass spectrometry (DEMS). Hydrogen gas evolution during the second cycle may originate from the reduction of crystalline water and the electrolyte at the anode, while the formation of CO_2 was related to the carbonate electrolyte at the cathode. If in a fully reversible reaction, the gas production of the active material generally didn't change as the reaction proceeds. However, the gas production in the first cycle differed from that in the second cycle. This discrepancy was caused by the side-reaction of hydrogen hexacyanide, which was presented in most PBAs. By setting the voltage range between 2.5 and 4.1 V, the generation of gas can be effectively suppressed by the suppression of previously mentioned side reactions through HE, which was still an issue in conventional PBAs. To better investigate the structural transformation during Na deintercalation and intercalation, *in situ* XRD analysis was performed in the first two cycles (Fig. 11c and d).[123,124] It could be found that the deintercalation process was fully reversible, and no phase transitions emerged throughout the reaction. Hence, the HE-PBA exhibited superior structural stability compared to traditional PBAs, providing additional evidence of the efficacy of the HE approach.

Ma *et al.* synthesized $Na_xMn_{0.4}Fe_{0.15}Ni_{0.15}Cu_{0.15}Co_{0.15}[Fe(CN)_6]$ (HE-MnPBAs). To understand the effect of entropy increase on the structure, they performed DFT calculations for several materials by using VASP and found that the formation energy of HEM-HCF HEMs was always the lowest. With the increase of ΔS_{config}, the formation energy decreased, leading to more stable materials. Compared with medium and low entropy

Table 1 Summary of the compositions and electrochemical performances of HE layered oxide cathodes

Cathode materials	Voltage range	Initial capacity (mA h g^{-1})	Cycle retention	Rate capacity (mA h g^{-1})	Ref.
$NaNi_{0.12}Cu_{0.12}Mg_{0.12}Fe_{0.15}Co_{0.15}Mn_{0.1}Ti_{0.1}Sn_{0.1}Sb_{0.04}O_2$	2–3.9 V	110	83% (500 cycles 3C)	86 (5C)	92
$Na_{0.7}Mn_{0.4}Ni_{0.3}Cu_{0.1}Fe_{0.1}Ti_{0.1}O_{1.95}F_{0.1}$	2–4.3 V	118.4	88.9% (200 cycles 2C)	108.5 (2C)	106
$Na_{2/3}Li_{1/6}Fe_{1/6}Co_{1/6}Ni_{1/6}Mn_{1/3}O_2$	2–4.5 V	171.2	63.7% (300 cycles 5C)	78.2 (10C)	107
$Na_{0.8}Li_{0.17}Ca_{0.025}Mg_{0.12}Ni_{0.05}Mn_{0.66}O_2$	2–4.3 V	163.6	80.43% (300 cycles 4C)	81 (4C)	108
$NaNi_{0.25}Mg_{0.05}Cu_{0.1}Fe_{0.2}Mn_{0.2}Ti_{0.1}Sn_{0.1}O_2$	2–4 V	130.8	75% (500 cycles 1C)	108 (5C)	109
$NaNi_{0.1}Mn_{0.15}Co_{0.2}Cu_{0.1}Fe_{0.1}Li_{0.1}Ti_{0.15}Sn_{0.1}O_2$	2–4.1 V	115	82.7% (1000 cycles 1C)	100 (8C)	110
$Na_{0.62}Mn_{0.67}Ni_{0.23}Cu_{0.05}Mg_{0.07}Ti_{0.01}O_2$	2–4.3 V	148.2	87% (500 cycles 1C)	59.3 (10C)	111
$Na_{0.9}Fe_{0.258}Co_{0.129}Ni_{0.258}Mn_{0.258}Ti_{0.097}O_2$	2–4.2 V	159.6	85.6% (100 cycles 2C)	110.1 (2C)	112
$NaCu_{0.1}Ni_{0.3}Fe_{0.2}Mn_{0.2}Ti_{0.2}O_2$	2–3.9 V	130	87.2% (100 cycles 0.1C)	85 (5C)	119
$NaMn_{0.2}Fe_{0.2}Co_{0.2}Ni_{0.2}Ti_{0.2}O_2$	1.5–4.2 V	180	97% (100 cycles 0.1C)	95 (2C)	115
$Na(Fe_{0.2}Co_{0.2}Ni_{0.2}Ti_{0.2}Sn_{0.1}Li_{0.1})O_2$	2–4.1 V	90.4	81% (100 cycles 0.5C)	81 (2C)	116
$NaNi_{0.2}Fe_{0.2}Mn_{0.35}Cu_{0.05}Zn_{0.1}Sn_{0.1}O_2$	2–4 V	128	87% (500 cycles 3C)	—	117
$NaNi_{0.3}Cu_{0.1}Fe_{0.2}Mn_{0.3}Ti_{0.1}O_2$	2–4 V	141.5	85% (500 cycles 1C)	120 (1C)	118

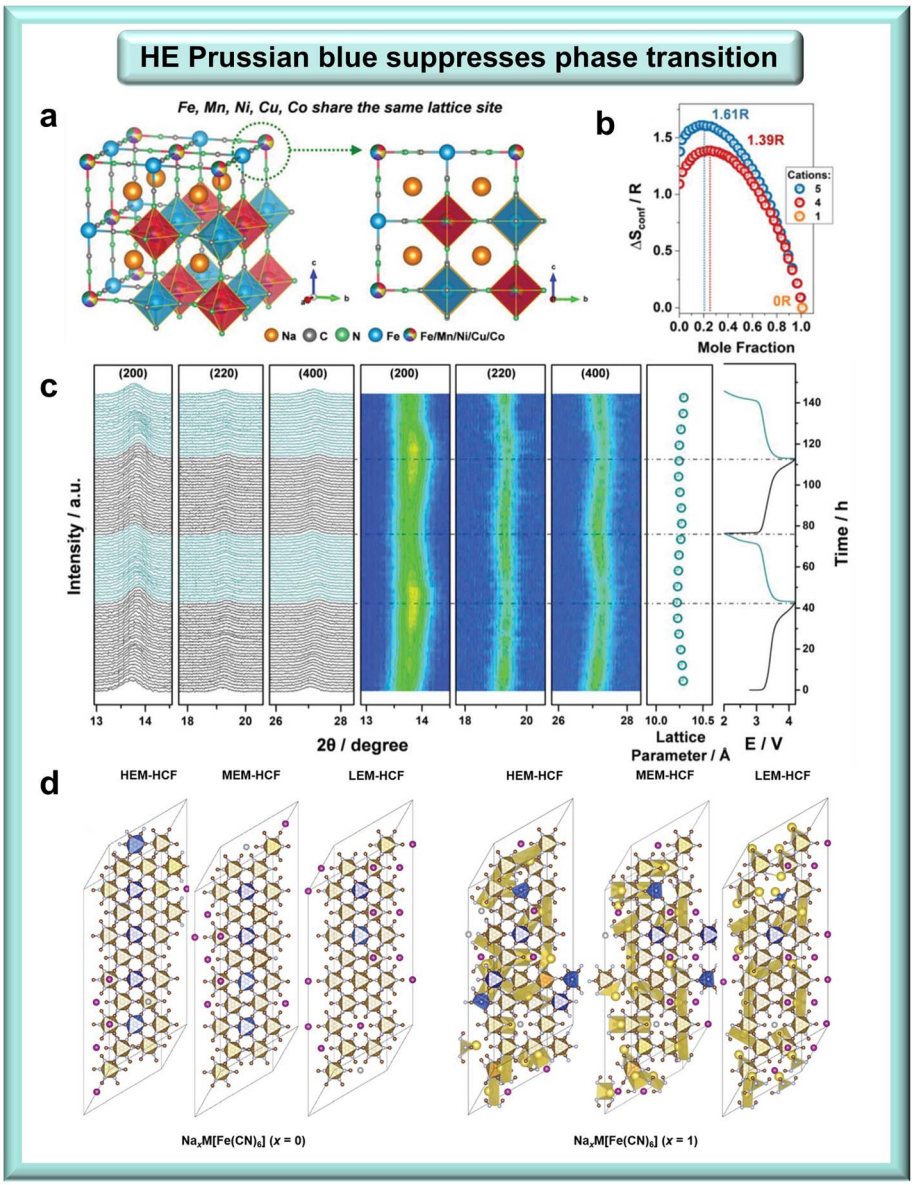

Fig. 11 (a) Schematic diagram of the crystal structure of multi-element doping. (b) *In situ* DEMS test of the HEM during the second charge/discharge. (c) *In situ* XRD patterns during charging and discharging. Reprinted with permission from ref. 95. Copyright 2021 Wiley VCH. (d) The structures of PBAs with three different entropies were simulated by using DFT calculations. Reprinted with permission from ref. 69. Copyright 2022 Wiley VCH.

samples, HEM-HCF exhibited a more stable structure during the reaction (Fig. 12a). The Mn K-edge analysis of HEM-HCF and Mn-HCF revealed that the half-path lengths of the M≡N, M≡C, and M≡M shells in both materials showed striking similarities. These findings indicated that the 4b (M) site (occupied by Fe, Mn, Co, Ni, and Cu) in each material shares an identical coordination environment with the Mn site, specifically –Fe(4a)–C≡N–M(4b)–N≡C–Fe(4a)–. Fe K-edge data for Mn-HCFs showed a comparable distribution of half-path lengths. Conversely, Fe-HCF presented a distinct first-shell layer distribution, characterized by discernible metal–ligand spacings, which highlighted the stability of its HE structure (Fig. 12b).[69]

As reported by Huang *et al.*, a HE monoclinic single-crystal Prussian blue analogue (SC-HEPBA) was prepared. The unique HE characteristic brought about rapid Na^+ diffusion and effectively suppressed metal dissolution. Additionally, the micron-scale single-crystal morphology enhanced the electrochemical performance and minimized structural deterioration during charge–discharge cycles.[125,126] As illustrated in Fig. 12c, the structural transformation of SC-HEPBA exhibited high reversibility during cycling. Fig. 12d further quantified the minimal volume change (3.3% during charge and 2.6% during discharge), which was attributed to the entropy-stabilized framework.[121] It could be inferred that this reverse three-phase transformation was caused by the structure formed by

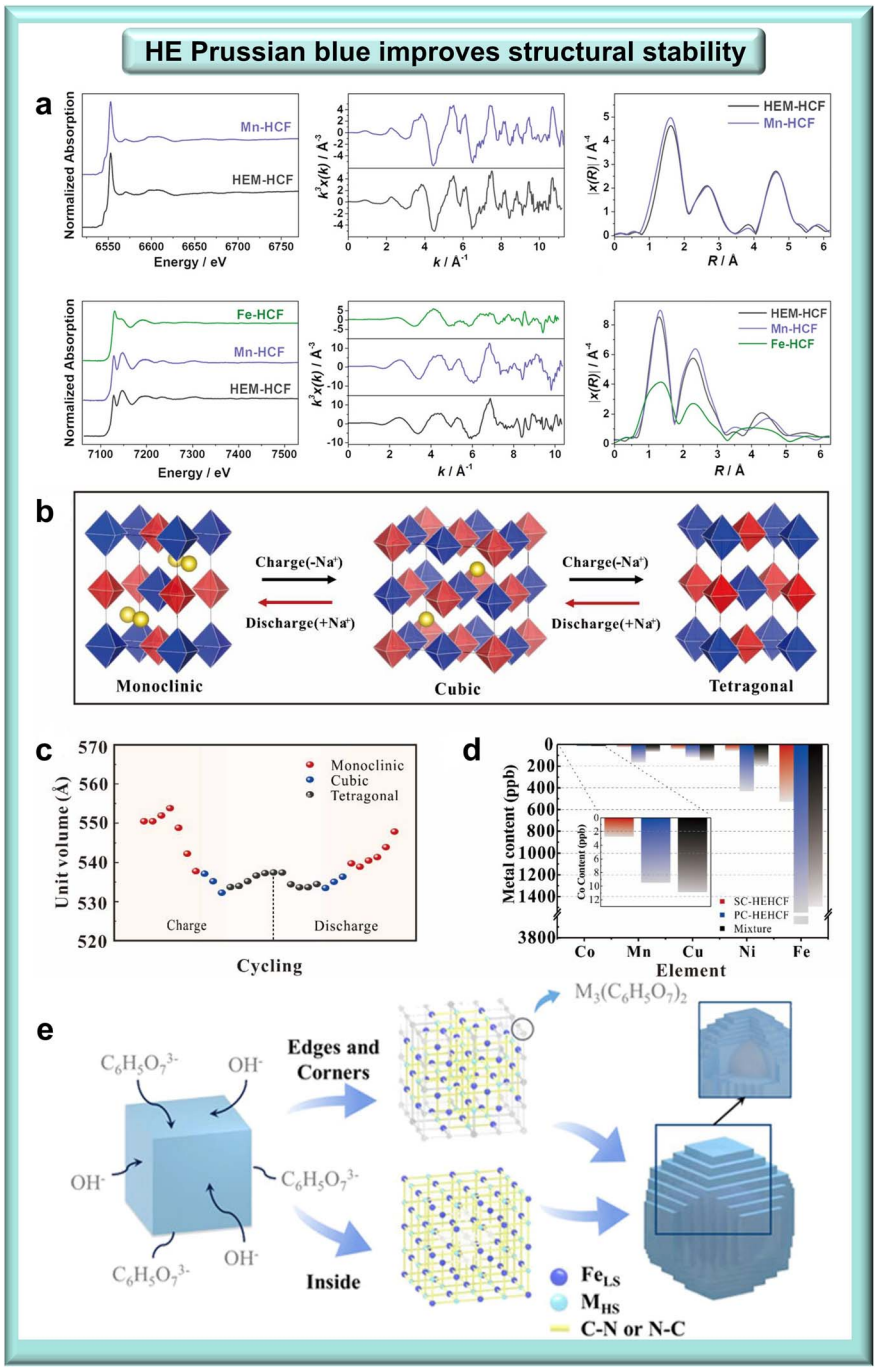

Fig. 12 (a) Comparison of XAS data for HEM and Mn-HCF. Comparison of XAS data for HEM, Mn-HCF, and Fe-HCF. Reprinted with permission from ref. 69. Copyright 2022 Wiley VCH. (b) Schematic diagram of the structural simulation of SC-HEPBA during the cycling process. (c) Schematic representation of the unit volume change of SC-HEPBA during charging and discharging. (d) The TM contents in the electrolyte after more than 100 cycles. Reprinted with permission from ref. 121. Copyright 2023 Elsevier. (e) Schematic diagram for the chemical etching process of HEPBA-Etched-0. Reprinted with permission from ref. 128. Copyright 2024 American Chemical Society.

using the single crystal strategy, and the relatively small volume change was attributed to the structure of HEPBAs. This structure greatly enhanced the Na^+ transport rate and ensured cycle stability of the material. The entropy-mediated capabilities of structural decay and phase transition were in the following order: low-entropy manganese-based PBAs were less than medium-entropy manganese-based PBAs, which were less than HE manganese-based PBA.

PBAs are regarded as competitive cathode materials for SIBs because of their low cost and ease of synthesis. Nevertheless, the practical application of PBA is restricted by its intrinsically poor electronic conductivity and structural degradation. Wang *et al.* integrated the benefits of HE and the 3D confinement effect provided by carbon wrapping (CW). For the first time, they designed and synthesized a distinctive three-dimensional carbon-wrapped HE-PBA (HE-PBA@C).[127] The HE strategy

guaranteed the inherent stability of PBA and facilitated Na^+ diffusion. Meanwhile, the CW technique had a dual function. It enhanced electronic conductivity through the 3D confinement effect and alleviated lattice distortion. Consequently, the HE-PBA@C cathode showed remarkable electrochemical performance. This included a high specific capacity (120.2 mA h g^{-1} at 10 mA g^{-1}), excellent rate performance (73.0 mA h g^{-1} at 4 A g^{-1}), outstanding capacity retention (80.1% after 4000 cycles at 2 A g^{-1}), and unprecedented stability under ambient conditions. Furthermore, in full cells, the HE-PBA@C cathode exhibited excellent compatibility with hard carbon (95.4% after 700 cycles) and $NaTi_2(PO_4)_3$ (98.1% after 1000 cycles) anodes. This highlighted its extensive potential for large-scale energy storage applications.

Introducing the HE concept into the PBAs structure further enhances its multiple performances. However, the severe agglomeration of HEPBA particles still limits its fast charging capacity. Zhang *et al.* prepared a HEPBA (Na_x(FeMnCoNiCu)$[Fe(CN)_6]_y\square_{1-y}\cdot nH_2O$) with a hollow stepped spherical structure by chemically etching the traditional cubic structure of HEPBA.[128] Electrochemical characterization, kinetic analysis, and COMSOL Multiphysics simulation showed that the HE nature and the hollow stepped spherical structure could greatly improve the diffusion behavior of Na^+. Moreover, the hollow structure effectively alleviated the volume change of HEPBA, ultimately extending its service life (Fig. 12e). Therefore, the prepared HEPBA cathode exhibited excellent rate performance (126.5 and 76.4 mA h g^{-1} at 0.1 and 4.0 A g^{-1}, respectively) and stable long-term performance (retaining 75.6% of its capacity after 1000 cycles), which was attributed to its unique structure. Additionally, the waste generated during the etching process could be easily recycled to prepare more HEPBA products. This processing method brings great hope for the design of advanced HE PBAs nanostructures for SIBs.

PBAs are promising SIB cathodes due to ease of synthesis and high Na^+ diffusivity. Nevertheless, irreversible structural alterations resulted from Jahn–Taller distortion cause performance decline, particularly in Fe/Mn-based PBAs. Additionally, disproportionation reactions lead to ion dissolution in acidic electrolytes. The HE approach alleviates rapid capacity fading caused by irreversible structural changes during cycling *via* the cocktail effect from multi-metal coordination and structural stabilization. The application of HE strategies in PBAs in recent years is summarized, and the significant role of HE in PBAs is demonstrated through the composition and electrochemical performance shown in Table 2.

3.3 HE polyanionic cathodes

Polyanion compounds are also crucial materials for a class of SIB cathodes, which have garnered attention of researchers due to their diverse types and unique sodium storage properties. Polyanionic materials are compounds characterized by the presence of multiple tetrahedral $(XO_4)^{n-}$ anion units, along with their derivative structures $(X_mO_{3m+1})^{n-}$ (where X can be S, P, Si, As, Mo, or W), and polyhedral MO_x units (with M denoting TMs) integrated into their framework.[129] In the majority of

Table 2 Summary of the compositions and electrochemical performances of HE Prussian blue analogue cathode

Cathode materials	Voltage range	Initial capacity (mA h g^{-1})	Cycle retention	Rate capacity (mA h g^{-1})	Ref.
$Na_{1.26}Mn_{0.4}Fe_{0.15}Ni_{0.15}Cu_{0.15}Co_{0.15}[Fe(CN)_6]_{0.81}\square_{0.19}\cdot 1.12H_2O$	2–4.1 V	117	90% (200 cycles 0.1 A g^{-1})	112 (0.1 A g^{-1})	69
$Na_{1.19}(Fe_{0.2}Mn_{0.2}Ni_{0.2}Cu_{0.2}Co_{0.2})[Fe(CN)_6]_{0.79}\square_{0.21}\cdot 1.16H_2O$	2–4.2 V	120	94% (150 cycles 0.1 A g^{-1})	96 (0.1 A g^{-1})	95
$Na_{1.70}Fe_{0.2}Mn_{0.2}Co_{0.2}Ni_{0.2}Cu_{0.2}[Fe(CN)_6]_{0.98}\square_{0.02}\cdot 2.35H_2O$	2–4 V	109.4	77.8% (2000 cycles 50 mA g^{-1})	96.5 (10C)	123
$Na_{1.41}Mn_{0.32}Fe_{0.11}Co_{0.28}Ni_{0.32}Cu_{0.32}[Fe(CN)_6]\cdot 2.89H_2O$	2–4.2 V	105.1	85.8% (200 cycles 1.5C)	92.6 (1.5C)	124
$Na_{1.36}Ni_{0.4}Fe_{0.15}Co_{0.15}Mn_{0.15}Cu_{0.15}[Fe(CN)_6]_{0.91}\square_{0.09}\cdot 1.18H_2O$	0–1.2 V	118.6	81.2% (1800 cycles 100 mA g^{-1})	90 (5C)	125
$Na_{1.65}Mn_{0.4}Fe_{0.12}Ni_{0.12}Cu_{0.12}Co_{0.12}Cd_{0.12}[Fe(CN)_6]_{0.92}\square_{0.08}\cdot 1.09H_2O$	1.5–4.2 V	129	98.7% (200 cycles 0.5 A g^{-1})	73 (0.5 A g^{-1})	126
$Na_{1.63}Mn_{0.40}Co_{0.22}Cu_{0.25}Ni_{0.06}Fe_{0.06}[Fe(CN)_6]_{0.92}\cdot 3.62H_2O$	2–4 V	120.2	80.1% (4000 cycles 2 A g^{-1})	75.1 (0.5 A g^{-1})	127
$Na_{1.816}Fe_{0.179}Mn_{0.215}Co_{0.215}Ni_{0.195}Cu_{0.196}[Fe(CN)_6]_{0.964}\square_{0.036}\cdot 2.443H_2O$	2–4.2 V	126.5	75.6% (1000 cycles 1 A g^{-1})	124 (0.1 A g^{-1})	128

polyanionic compounds, the $(XO_4)^{n-}$ anion group facilitates fast ion conduction within an open-framework structure while also stabilizing the redox couples of TMs. A comparison of polyanionic compounds with oxide materials and other cathode materials reveals several noteworthy advantages. These include robust three-dimensional architectures, broad voltage windows, and enhanced safety profiles.[130] For instance, phosphate materials exhibit high thermal stability due to their P–O covalent bonds. It is a well-documented phenomenon that layered oxides typically undergo decomposition at temperatures exceeding

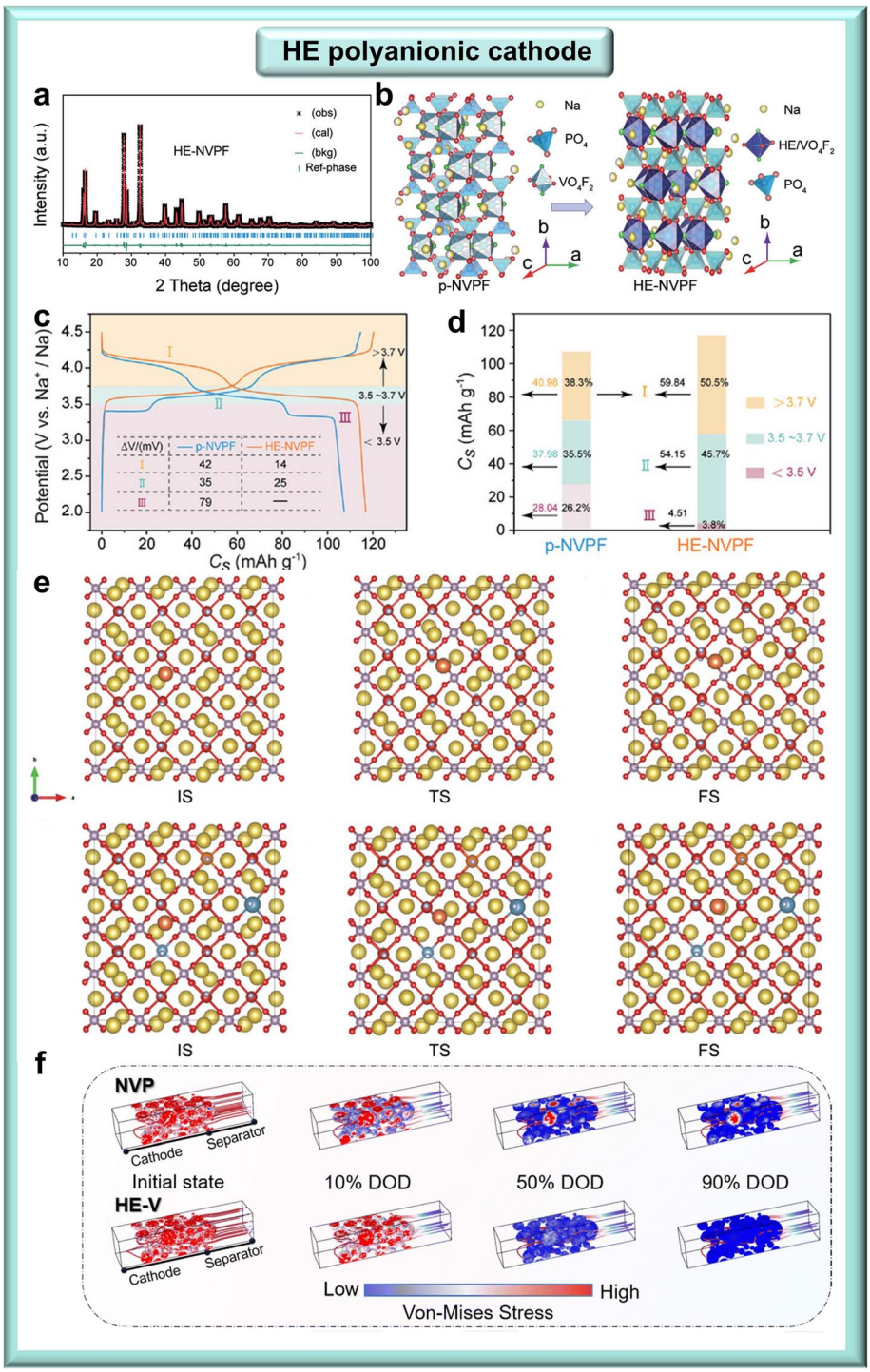

Fig. 13 (a) The XRD pattern of HE-NVPF. (b) The structures of p-NVPF and HE-NVPF. (c) GCD curves within the potential window of 2.0–4.3 V. (d) Cs values and capacity contributions during discharge. (e) Na^+ migration pathways in p-NVPF. Reprinted with permission from ref. 78. Copyright 2022 Wiley VCH. COMSOL simulation and postmortem analysis. (f) Stress field analysis at different depths of discharge (DOD) states based on the COMSOL platform. Reprinted with permission from ref. 128. Copyright 2025 RSC.

200 °C, resulting in the release of oxygen. However, the covalent bond in polyanionic compounds has been shown to effectively inhibit this process. Nevertheless, compared with layered oxides and Prussian blue counterparts, polyanions generally exhibit poor conductivity.[131] To overcome this challenge, a carbon coating is commonly used to modify the surface of polyanions, which enhances their conductivity to some extent. Another major challenge associated with polyanion compounds is their strong water absorption property. When exposed to the air, they will spontaneously react with water to form residual alkali such as sodium hydroxide. Furthermore, uneven material surfaces may adversely affect the electrochemical performance of the electrode. The HE strategy holds great potential for developing high-performance polyanionic materials.

As shown in Fig. 13a, HE-NVPF exhibited excellent crystallinity, demonstrating a strong correlation with tetragonal structures belonging to the space group $P4_2/mnm$. The six cations were randomly dispersed among the 8j sites. Fig. 13b showed the schematic structures of $Na_3V_2(PO_4)_2F_3$ (p-NVPF) and $Na_3V_{1.9}$(Ca, Mg, Al, Cr, Mn)$_{0.1}(PO_4)_2F_3$ (HE-NVPF), which exhibited an open architecture.[78] As shown in Fig. 13c and d, the HE effect significantly enhanced the operating voltage, which in turn boosted the discharge capacity of the NVPF cathode and mitigated adverse effects during low-voltage discharge. Within the NVPF structure, there were two types of sodium sites, Na (1) and Na (2). The Na (1) sites demonstrated minimal electrochemical activity and didn't participate in redox reactions, while the Na (2) sites were highly electrochemically active, facilitating Na^+ intercalation/deintercalation. In the HE structure, the proportion of Na (2) sites increased from 50% to 60.2%. This implied that the diffusion rate of Na^+ was enhanced. Due to the substantial accumulation of Na^+ at the Na (2) sites, the Na^+ concentration at the Na (1) sites decreased. The Na (2) sites could more efficiently facilitate the rearrangement of Na^+, thereby effectively suppressing phase transition. As shown visually in Fig. 13e, it depicted the migration path of Na^+ moving from the Na (2) site to the Na (1) site in both p-NVPF and HE-NVPF. In these diagrams, IS represented the initial state, TS standed for the transition state, and FS indicated the final state. The computed energy barriers for sodium migration were 1.984 eV for p-NVPF and 0.963 eV for HE-NVPF. Notably, HE-NVPF exhibited significantly lower migration barriers than p-NVPF, which enhanced the diffusion of Na^+. Furthermore, the final state energy of HE-NVPF (0.5370 eV) was considerably lower than that of p-NVPF (1.6750 eV). This suggested that Na^+ in the HEM exhibited a greater tendency to escape, thereby reducing the likelihood of Na site rearrangement and inhibiting reactive phase transitions in the low-voltage region.[133–136] The feasibility of the HE approach was further verified. The HE structure significantly enhanced the low-voltage discharge plateau of the material, providing a higher operating voltage and increased energy density. Meanwhile, the highly stable structure achieved through structural regulation delivered good cycling stability (2000 cycles at 2C with 80% capacity retention), suppressed the irreversible phase transition, and induced the escape of Na^+ from the Na (2) site. This provided valuable inspiration for the design of SIB cathodes.

For the advancement of high-performance NASICON-type cathode materials for SIBs, it is of great significance to prevent severe structural deformation and irreversible phase transition, as well as to achieve stable multi-electron redox reactions.[133,134] Du *et al.* synthesized a high-entropy $Na_{3.45}V_{0.4}$-$Fe_{0.4}Ti_{0.4}Mn_{0.45}Cr_{0.35}(PO_4)_3$ (HE-$Na_{3.45}$TMP) cathode material *via* ultrafast high-temperature shock treatment.[137] This method effectively reduced the likelihood of phase separation and enabled reversible and stable multi-electron transfer of 2.4/2.8 e^- with respect to Na^+/Na within the voltage ranges of 2.0–4.45/1.5–4.45 V, corresponding to capacities of 137.2/162.0 mA h g^{-1}. Constant current charge–discharge experiments and *in situ* X-ray diffraction tests demonstrated the continuous redox reaction and approximate solid solution phase transition process of HE-$Na_{3.45}$TMP. DFT calculations were carried out to analyse the migration pathways and energy barriers, further validating the superior reaction kinetics of HE-$Na_{3.45}$TMP. Consequently, HE-$Na_{3.45}$TMP showed outstanding wide-temperature adaptability and could operate stably in the temperature range from −50 to 60 °C. After 400 cycles at −40 °C, the capacity retention rate reached up to 92.8%, and it could still maintain a capacity of 73.7 mA h g^{-1} at −50 °C. The assembled hard carbon//HE-$Na_{3.45}$TMP full cell offered an energy density of approximately 301 Wh kg^{-1}, which verified the application feasibility of HE-$Na_{3.45}$TMP. This work provided an innovative and ultrafast approach for the rational fabrication of high-performance cathodes for SIBs.

Dong *et al.* prepared spherical HE $Na_4Fe_{2.95}$(-MgCaAlCrMn)$_{0.01}(PO_4)_2P_2O_7$ (HE-NFPP) cathode materials *via* spray drying in combination with solid-state reaction.[138] By adopting the HE approach, the co-doping of TMs in NFPP could effectively mitigate volume variations. This was achieved by decreasing the band gap between the conduction band and the valence band, which in turn improved its electronic conductivity. Additionally, through the HE strategy, the co-doping of TM ions in NFPP creates three-dimensional network Na^+ ion diffusion channels. These channels were beneficial for Na^+ ion diffusion, thus enhancing the electrode reaction kinetics at low temperatures.

NASICON-type compounds possess the advantages of rapid Na^+ diffusion and structural stability. Nevertheless, they still suffer from several drawbacks, such as a low specific capacity (less than 120 mA h g^{-1}) and significant volume changes. HE engineering is a method aimed at enhancing structural and functional stability by using multiple dopants. This strategy has demonstrated great potential in layered oxides. However, applying it to NASICON is inherently difficult because of the rigid poly-anionic framework, dopant incompatibility, and redox mismatch. Zhang *et al.* presented an entropy-stabilized NASICON cathode, namely $Na_{3.2}V_{1.5}Cr_{0.1}Mn_{0.1}Fe_{0.1}Al_{0.1}Mg_{0.1}$(-$PO_4)_3$ (HE-V).[139] It was synthesized *via* complex doping at the 12c Wyckoff site. The HE method enabled the fabrication of single-phase materials with enhanced redox flexibility and decreased lattice strain. The HE-V material was able to reach a high reversible capacity of 170 mA h g^{-1} by means of multi-electron $V^{5+}/V^{4+}/V^{3+}/V^{2+}$ redox reactions. Additionally, it exhibited outstanding rate performance and cycling stability, retaining its

Table 3 Summary of the compositions and electrochemical performances of HE polyanionic cathodes

Cathode materials	Voltage range	Initial capacity (mA h g^{-1})	Cycle retention	Rate capacity (mA h g^{-1})	Ref.
$Na_3V_{1.9}(Ca,Mg,Al,Cr,Mn)_{0.1}(PO_4)_2F_3$	2–4.3 V	118.5	80.4% (2000 cycles 20C)	71.4 (50C)	78
$Na_4Fe_{2.85}(Ni,Co,Mn,Cu,Mg)_{0.03}(PO_4)_2P_2O_7$	1.5–4.2 V	122	82.3% (1500 cycles 10C)	85 (50C)	132
$Na_4Fe_{2.95}(NiCoMnMgZn)_{0.01}(PO_4)_2P_2O_7$	1.5–4.2 V	124.6	93% (5000 cycles 20C)	82.7 (1C)	133
$Na_4Fe_{2.5}Mn_{0.1}Mg_{0.1}Co_{0.1}Ni_{0.1}Cu_{0.1}(PO_4)_2(P_2O_7)$	1.4–4.0 V	108.9	99.2% (200 cycles 1 A g^{-1})	55.0 (10 A g^{-1})	134
$Na_{3.12}MnTi_{0.9}(VFeMgCrZr)_{0.02}(PO_4)_3$	1.5–4.3 V	169.6	81.7% (1000 cycles 5C)	132.3 (1C)	135
$Na_{3.6}VMn_{0.4}Fe_{0.4}Ti_{0.1}Zr_{0.1}(PO_4)_3$	1.5–4.3 V	110	80.6% (10 000 cycles 10C)	78.5 (20C)	136
$Na_{3.45}V_{0.4}Fe_{0.4}Ti_{0.4}\ Mn_{0.45}Cr_{0.35}(PO_4)_3$	1.5–4.45 V	162	83.7% (2000 cycles 5C)	73.7 (5C)	137
$Na_4Fe_{2.95}(NiCoMnMgZn)_{0.01}(PO_4)_2P_2O_7$	1.7–4.3 V	106.5	92.0% (1000 cycles 1C)	67.1 (50C)	138
$Na_{3.2}V_{1.5}Cr_{0.1}Mn_{0.1}Fe_{0.1}Al_{0.1}Mg_{0.1}(PO_4)_3$	1.5–4.1 V	170	93.3% (10 000 cycles 50C)	160 (0.2C)	139

performance after over 10 000 cycles at 50C. Both *in situ* and *ex situ* characterizations demonstrated near-zero strain structures, low defect generation, and strengthened local bonding (Fig. 13f). Theoretical computations further confirmed a narrowed bandgap and improved charge transport. This study had created a new type of HE polyanionic cathodes, overcoming long-standing constraints in NASICON chemistry and providing a practical path for the development of long-lasting and high-energy SIBs.

Polyanion cathodes, characterized by three-dimensional framework architectures and distinctive tetrahedral PO_4 units, exhibit remarkable structural stability and a high operating voltage. However, the relatively low electronic conductivity of these polyanion cathode materials severely undermines their electrochemical performances. For instance, they display a low specific capacity and inferior rate performance. The HE approach enhances the energy density and extends the cycle life of the polyanionic cathode through multi-scale coordination, structural stabilization, and dynamic optimization. In the future, the relationship between element ratios and synthesis processes can be further explored, and the optimal HE combination can be predicted using machine learning. In addition, interface-volume phase multi-scale entropy regulation and the development of wide-voltage-window electrolytes will be the key directions to improve the performance of the entire battery. Based on the electrochemical performance of HE polyanion cathodes reported so far, which is summarized in Table 3, the HE doping strategy plays a significant role in enhancing the specific capacity and cycling stability of polyanion cathodes. However, research in this field is still in its early stages and requires further efforts.

4 Summary and outlook

The HE approach broadens the design possibilities for SIBs and expedites the advancement of sophisticated Na storage materials, garnering increasing global attention and undergoing extensive research efforts. However, certain aspects remain underdeveloped. There are ongoing debates surrounding its functional mechanism, indicating that researchers' understanding of HEMs is still in its nascent stage.[140] While further investigations are currently underway to explore the structure–performance relationship of HEMs, numerous questions and challenges persist.

4.1 Reasonable designs of HEMs

The compositional complexity of HEMs not only forms the basis for their favorable electrochemical performance but also poses challenges in material design. There are two key aspects to consider when designing high-performance HEMs: selecting proper elements and optimizing the stoichiometry of components. HEMs have stringent requirements for element selection, which are determined by structural and functional criteria. Structural criteria encompass factors such as ionic size, valence state, chemical compatibility, and redox behavior.[141] For multiple elements to share the same crystallographic position, they need to have comparable ionic sizes to ensure electrical balance. Furthermore, it is important to prevent charge exchange between coexisting elements. For example, the formation of reduced Mn^{2+} and oxidized V^{5+} from Mn^{3+} and V^{3+} at the same crystallographic site should be prevented.[142–144] Therefore, during the selection process, cation pairs that are incompatible in terms of redox reactions should be excluded. Functional criteria focus on how different elemental groups affect the electrochemical processes involved. When considering the stoichiometry of components, a balance must be struck between achieving HE and maintaining high capacity. Introducing extra cationic elements can lower the concentration of redox-active components, which in turn decreases the overall capacity. Additionally, higher proportions of specific element species, such as Ti^{4+} and Zn^{2+}, can influence this relationship significantly, poor compatibility with other ions may result in the formation of secondary phases. Hence, achieving a balance among these factors is crucial when designing HEMs.

4.2 Theoretical calculations

The theoretical investigation of battery materials predominantly employs DFT and molecular dynamics (MD).[145,146] However, given the inherent disorder and complexity associated with HE systems, conventional theoretical calculation methodologies encounter significant challenges. Therefore, it is imperative to develop and implement more appropriate computational methodologies.[147–149] In recent years, many

scholars have found that machine learning (ML),[150–155] hybrid Monte Carlo (MC), and high-throughput computing (HTC) can be applied to HEBM systems because these methods are faster and simpler than traditional computing methods.[156–158] Although some computational methods are primarily applied to traditional HEA materials, ML, MC, HTC, DFT, and MD can be integrated to optimize the structure and atomic configuration of HEMs. Rao *et al.* took advantage of the active learning cycle characteristics of machine learning and combined them with methods such as DFT, experiments, and thermodynamic calculations to successfully select two HEAs with complex compositions from millions of potential candidates.[159] Kaufmann *et al.* used a high-throughput machine learning model to predict the formation of face-centered cubic and body-centered cubic solid solutions from thousands of quaternary and quinary components, and the prediction accuracy could be continuously improved.[160] The results of such theoretical work can be used for experimental verification. Then, the structure, morphology, electrochemical properties, charge compensation, and phase evolution of the material can be measured experimentally. Finally, the most promising HEMs are selected, and the information is fed back to the HEMs database. With the advancement of HE composite materials, the potential for battery applications is significant, and the combination of these computational methods plays a crucial role. The diversity of HEMs opens up multiple approaches to the design of battery materials. Although the above computational methods have great potential in the field of HE alloys, their application in the field of SIBs requires further improvement in terms of accuracy. Therefore, while optimizing traditional computational methods, it is essential to continuously improve the underlying

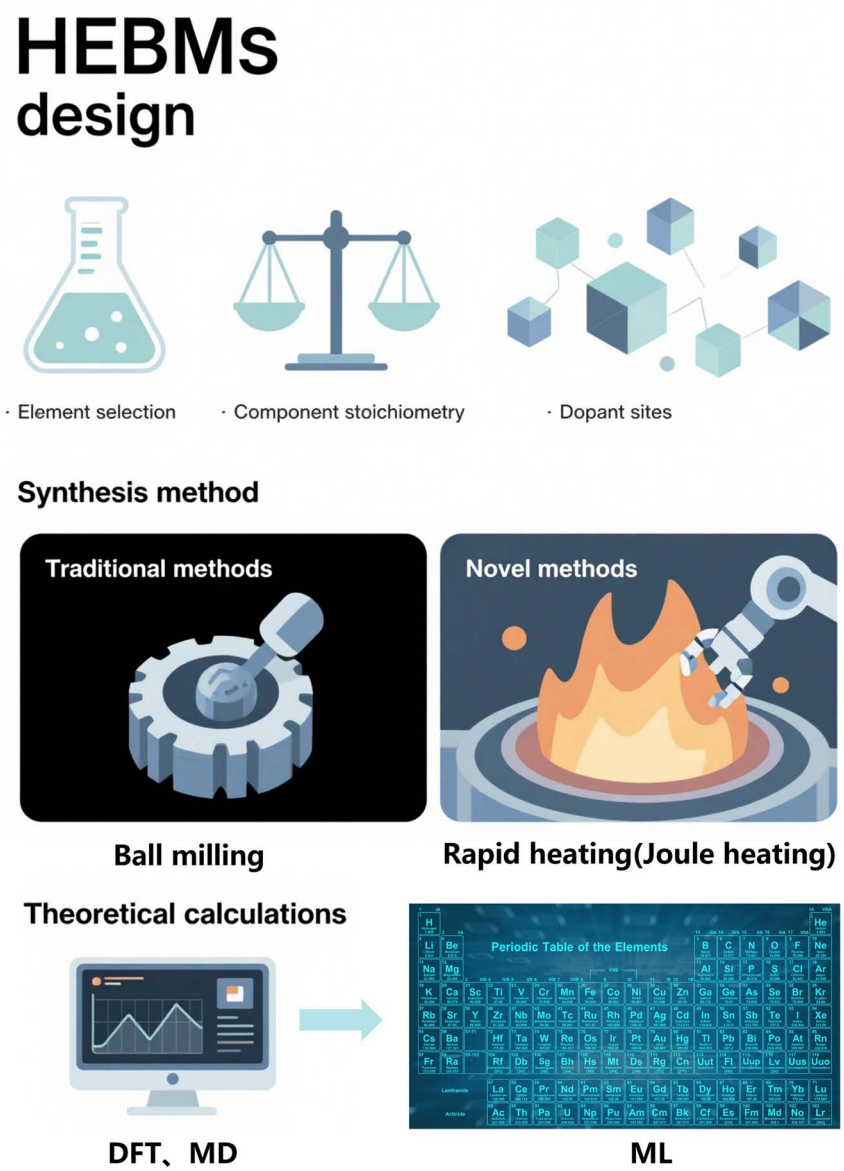

Fig. 14 The research content and an overview of HEMs are presented.

theory. Learning and applying new methods from related fields is also essential.

4.3 Applications of HE strategy

To date, the operational principles of HEMs have predominantly been evaluated based on their outcomes, resulting in limited understanding and ongoing disputes about their enhancement mechanisms. A deeper comprehension of structural distortions within HEMs necessitates more extensive structural analysis across various length scales. While many studies attribute the improved electrochemical performance of HEMs to the synergistic interactions among multiple elements, the specific mechanisms and differential impacts of these elements remain largely undefined. Additionally, incorporating multiple elements can induce substantial lattice distortions in the crystal structure.[161–163] While studies exploring the connection between distortion levels and electrochemical performance from atomic, lattice, stacking fault, and strain perspectives are still limited, future research should focus on elucidating the roles of individual elements during cycling and their correlation with the compound's properties. At present, the HE strategy mainly focuses on improving battery materials by introducing multi-element doping into the crystal structure. It has been found that phenomena at the electrode/electrolyte interface, such as the dissolution of TMs and their poor interaction with the electrolyte, can have a negative impact on electrochemical performance.[164,165] Researchers have pointed out that existing reports on high energy density materials mainly revolve around modification methods, but often neglect factors such as synthesis methods, particle morphology and size, which are important for further research in the fields such as scale-up production. Therefore, more efforts are needed to optimize these parameters to obtain high energy density materials with excellent electrochemical performance. Finally, in recent years, adjusting ΔS_{config} to regulate the electrochemical performance of materials has become a research hotspot. More attentions should be paid to clarifying the relationship between ΔS_{config} and electrochemical performance to better guide the development of HE cathode materials (Fig. 14).

In conclusion, HE approach offers a revolutionary method for developing advanced materials for SIBs, which dramatically improves the ΔS_{config} and effectively contributes to the design of battery materials. This review summarizes the underlying mechanisms and highlights six advantages of HEMs. HEMs can be seen as extensions of four effects observed in HEAs: (1) reduced volume strain, (2) inhibited adverse phase transitions, (3) facilitated conversion processes, (4) improved ion transport, (5) enhanced disordered ion diffusion, and (6) cocktail-induced synergistic mechanisms. These advantages are not mutually exclusive, instead, multiple research advantages may coexist within a single HEBM. Furthermore, this review establishes a composition–structure–dynamics framework that integrates HE design principles with electrochemical performance across SIB cathodes (Fig. 15). Departing from static configurations, we emphasize operationally adjustable entropy as a dynamic lever to optimize material behavior. By synthesizing recent advances

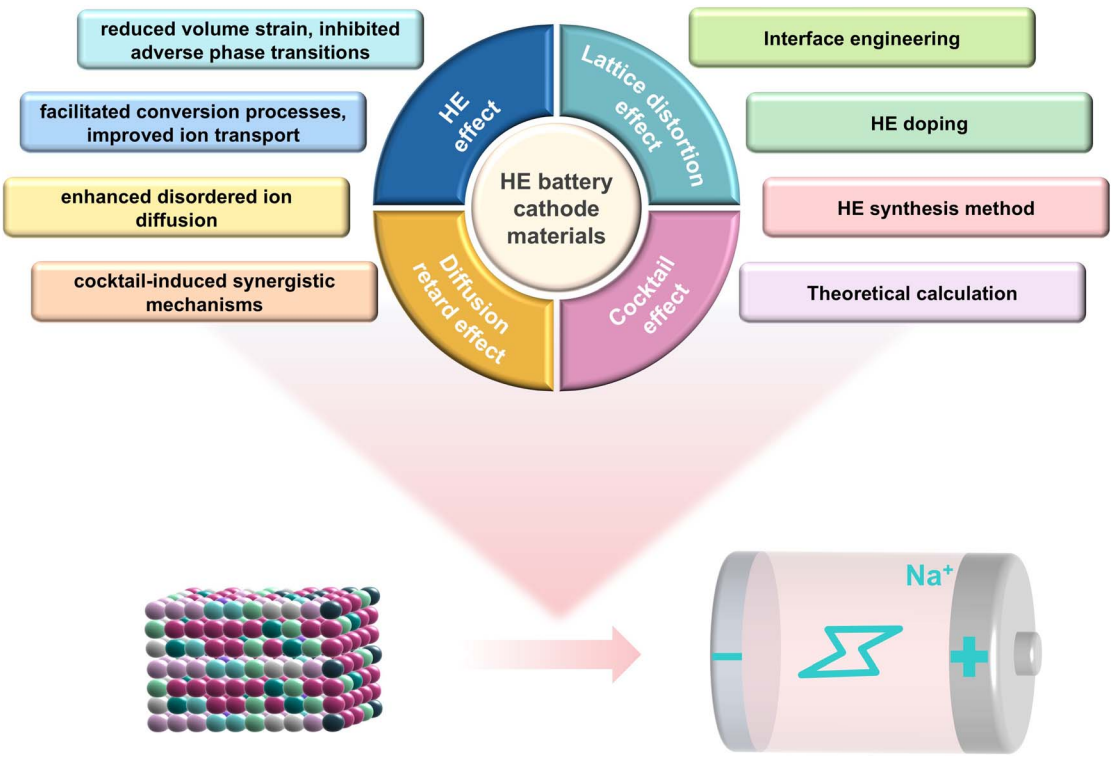

Fig. 15 The application of HE strategies in the field of SIBs is summarised on the left, while the future research directions that require to be explored are showed on the right.

in layered oxides, PBAs, and polyanionic systems, demonstrate how HEMs mitigate lattice distortion, suppress phase transitions, and enhance Na^+ diffusion kinetics through multi-element synergies. This study further proposed the design standards for entropy-driven cathode engineering, outlined the current challenges and the future research directions for HE cathodes. This framework provides actionable insights for developing next-generation SIBs.

Author contributions

Zhuozheng Hong: conceptualization, literature curation, writing-original draft. Zhuang-Chun Jian: methodology, manuscript revision. Yan-Fang Zhu: conceptualization, methodology, data analysis, manuscript revision. Hanshen Xin: project administration. Yan-Jiang Li: manuscript revision. Qi-Cong Ling: methodology, data curation. Didi Wang: methodology, data curation. Chao Wu and Yao Xiao: supervision, funding acquisition.

Conflicts of interest

The authors declare no conflict of interest.

Data availability

No primary research results, software or code have been included and no new data were generated or analyzed as part of this review.

Acknowledgements

This work was financially supported by the National Natural Science Foundation of China (52402301, 52472240, 52202284), Natural Science Foundation of Zhejiang Province (LQ23E020002), Wenzhou Key Scientific and Technological Innovation Research Project (ZG2023053).

References

1 A. Gao, X. Li, Q. Zhang, T. Lin, Y. Wang, Y. Chen, W. Lin, S. Wang, P. Ji, Z. Luo, J. Wang, Y. Guo and L. Gu, *Adv. Mater.*, 2025, **37**, e2412673.
2 X. Lu, S. Li, Y. Li, F. Wu, C. Wu and Y. Bai, *Adv. Mater.*, 2024, **36**, e2407359.
3 X. Rong, D. Xiao, Q. Li, Y. Niu, F. Ding, X. Hou, Q. Wang, J. Xu, C. Zhao, D. Zhou, R. Xiao, X. Yu, W. Yin, L. Gu, H. Li, X. Huang, L. Chen and Y.-S. Hu, *eScience*, 2023, **3**, 100159.
4 C. Jiang, Y. Wang, Y. Xin, X. Ding, S. Liu, Y. Pang, B. Chen, Y. Wang, L. Liu, F. Wu and H. Gao, *Carbon Neutralization*, 2024, **3**, 233–244.
5 Z. Zhu, T. Jiang, M. Ali, Y. Meng, Y. Jin, Y. Cui and W. Chen, *Chem. Rev.*, 2022, **122**, 16610–16751.
6 H. Chen, H. Yuan, Z. Dai, S. Feng, M. Zheng, C. Zheng, J. Jin, M. Wu, X. Wu, J. Lu, Y. Lu and Z. Wen, *Adv. Mater.*, 2024, **36**, e2401052.
7 Z. Dai, Y. Liu, X. Lu, H. Zhao and Y. Bai, *Adv. Mater.*, 2024, **36**, e2313500.
8 Q. Huang, J. Liu, X. Chen, P. Zhang, L. Lu, D. Ren, M. Ouyang and X. Liu, *Adv. Mater.*, 2025, **37**, e2410006.
9 H. Li, L. Wang, Y. Song, Z. Zhang, A. Du, Y. Tang, J. Wang and X. He, *Adv. Mater.*, 2024, **36**, e2312292.
10 X. Zhu, A. Huang, I. Martens, N. Vostrov, Y. Sun, M. I. Richard, T. U. Schulli and L. Wang, *Adv. Mater.*, 2024, **36**, e2403482.
11 T. Yang, K. Zhang, Y. Zuo, J. Song, Y. Yang, C. Gao, T. Chen, H. Wang, W. Xiao, Z. Jiang and D. Xia, *Nature Sustainability*, 2024, **7**, 1204–1214.
12 L. Zhu, M. Wang, S. Xiang, D. Sun, Y. Tang and H. Wang, *Adv. Energy Mater.*, 2023, **13**, 2302046.
13 Y. Li, H. Jia, U. Ali, H. Wang, B. Liu, L. Li, L. Zhang and C. Wang, *Adv. Energy Mater.*, 2023, **13**, 2301643.
14 F. Karcher, M. Uhl, T. Geng, T. Jacob and R. Schuster, *Angew. Chem., Int. Ed.*, 2023, **62**, e202301253.
15 Y. Niu, Y. Zhao and M. Xu, *Carbon Neutralization*, 2023, **2**, 150–168.
16 H. Liu, L. Kong, H. Wang, J. Li, J. Wang, Y. Zhu, H. Li, Z. Jian, X. Jia, Y. Su, S. Zhang, J. Mao, S. Chen, Y. Liu, S. Chou and Y. Xiao, *Adv. Mater.*, 2024, **36**, e2407994.
17 Y. F. Liu, H. X. Liu, Y. F. Zhu, H. R. Wang, J. Y. Li, Y. C. Li, H. Y. Hu, Z. G. Wu, X. D. Guo and Y. Xiao, *Adv. Mater.*, 2025, **37**, e2417540.
18 L. Y. Kong, J. Y. Li, H. X. Liu, Y. F. Zhu, J. Wang, Y. Liu, X. Y. Zhang, H. Y. Hu, H. Dong, Z. C. Jian, C. Cheng, S. Chen, L. Zhang, J. Z. Wang, S. Chou and Y. Xiao, *J. Am. Chem. Soc.*, 2024, **146**, 32317–32332.
19 Y. Niu, Z. Hu, H. Mao, L. Zhou, L. Wang, X. Lou, B. Zhang, D. Xiao, Y. Yang, F. Ding, X. Rong, J. Xu, W. Yin, N. Zhang, Z. Li, Y. Lu, B. Hu, J. Lu, J. Li and Y.-S. Hu, *Energy Environ. Sci.*, 2024, **17**, 7958–7968.
20 W. Huang, S. Wang, X. Zhang, Y. Kang, H. Zhang, N. Deng, Y. Liang and H. Pang, *Adv. Mater.*, 2023, **35**, e2310147.
21 R. Hou, S. Guo and H. Zhou, *Adv. Energy Mater.*, 2023, **13**, 2300053.
22 S. L. Fereja, Z. Zhang, Z. Fang, J. Guo, X. Zhang, K. Liu, Z. Li and W. Chen, *ACS Appl. Mater. Interfaces*, 2022, **14**, 38727–38738.
23 Y. Wang, X. Y. Zhang, H. He, J. J. Chen and B. Liu, *Adv. Energy Mater.*, 2023, **14**, 2303923.
24 M. Xie, X. Xiao, D. Wu, C. Zhen, C. Wu, W. Wang, H. Nian, F. Li, M. D. Gu and Q. Xu, *Nano Res.*, 2024, **17**, 5288–5297.
25 M. Tamtaji, M. G. Kim, J. Wang, P. R. Galligan, H. Zhu, F. F. Hung, Z. Xu, Y. Zhu, Z. Luo, W. A. Goddard and G. Chen, *Adv. Sci.*, 2024, **11**, e2309883.
26 D. Du, H. He, R. Zheng, L. Zeng, X. Wang, C. Shu and C. Zhang, *Adv. Energy Mater.*, 2024, **14**, 2304238.
27 J. Mu, T. Cai, W. Dong, C. Zhou, Z. Han and F. Huang, *Chem. Eng. J.*, 2023, **471**, 144403.
28 Y. Ma, Y. Ren, D. Sun, B. Wang, H. Wu, H. Bian, J. Cao, X. Cao, F. Ding, J. Lu and X. Meng, *J. Mater. Sci. Technol.*, 2024, **188**, 98–104.
29 A. Chatterjee, D. Ganguly, R. Sundara and S. S. Bhattacharya, *Energy Technol.*, 2023, **12**, 2300576.

30 Y. Wang, M. J. Robson, A. Manzotti and F. Ciucci, *Joule*, 2023, **7**, 848–854.
31 Z.-Y. Liu, Y. Liu, Y. Xu, H. Zhang, Z. Shao, Z. Wang and H. Chen, *Green Energy Environ.*, 2023, **8**, 1341–1357.
32 B. Ouyang and Y. Zeng, *Nat. Commun.*, 2024, **15**, 973.
33 B. Ran, H. Li, R. Cheng, Z. Yang, Y. Zhong, Y. Qin, C. Yang and C. Fu, *Adv. Sci.*, 2024, **11**, 2401034.
34 J. M. Gonçalves, É. A. Santos, P. R. Martins, C. G. Silva and H. Zanin, *Energy Storage Mater.*, 2023, **63**, 102999.
35 S. Lee, L. Bai, J. Jeong, D. Stenzel, S. Schweidler and B. Breitung, *Electrochim. Acta*, 2023, **463**, 142775.
36 C. Jiang, Y. Wang, Y. Xin, X. Ding, S. Liu, Y. Pang, B. Chen, Y. Wang, L. Liu, F. Wu and H. Gao, *Carbon Neutralization*, 2024, **3**, 233–244.
37 Z.-C. Jian, Y.-F. Liu, Y.-F. Zhu, J.-Y. Li, H.-Y. Hu, J. Wang, L.-Y. Kong, X.-B. Jia, H.-X. Liu, J.-X. Guo, M.-Y. Li, Y.-S. Xu, J.-F. Mao, S.-L. Zhang, Y. Su, S.-X. Dou, S.-L. Chou and Y. Xiao, *Nano Energy*, 2024, **125**, 109528.
38 Y. Ma, Y. Ma, Q. Wang, S. Schweidler, M. Botros, T. Fu, H. Hahn, T. Brezesinski and B. Breitung, *Energy Environ. Sci.*, 2021, **14**, 2883–2905.
39 B. Jiang, Y. Yu, J. Cui, X. Liu, L. Xie, J. Liao, Q. Zhang, Y. Huang, S. Ning, B. Jia, B. Zhu, S. Bai, L. Chen, S. J. Pennycook and J. He, *Science*, 2021, **371**, 830–834.
40 E. P. George, D. Raabe and R. O. Ritchie, *Nat. Rev. Mater.*, 2019, **4**, 515–534.
41 L. Huang, J. Zhu, J.-X. Liu, H. Wu and G.-J. Zhang, *J. Adv. Ceram.*, 2024, **13**, 1093–1118.
42 C. M. Rost, E. Sachet, T. Borman, A. Moballegh, E. C. Dickey, D. Hou, J. L. Jones, S. Curtarolo and J. P. Maria, *Nat. Commun.*, 2015, **6**, 8485.
43 Z.-C. Jian, W. Shi, Y. Liu, X. Li, J.-Y. Li, Y.-F. Zhu, X. Zhu, Y. Li, P. Tan, P.-F. Wang, S. Chen, S. Zhang, J. Mao, G. Zhou, X.-D. Guo, J. Wang, S. X. Dou and Y. Xiao, *Energy Environ. Sci.*, 2025, **18**, 7995–8008.
44 X. Xu, Y. Huang, D. Li, Q. Pan, S. Hu, Y. Li, H. Wang, Y. Huang, F. Zheng and Q. Li, *J. Energy Chem.*, 2023, **81**, 200–211.
45 D. Bérardan, S. Franger, A. K. Meena and N. Dragoe, *J. Mater. Chem. A*, 2016, **4**, 9536–9541.
46 A. Sarkar, L. Velasco, D. Wang, Q. Wang, G. Talasila, L. de Biasi, C. Kubel, T. Brezesinski, S. S. Bhattacharya, H. Hahn and B. Breitung, *Nat. Commun.*, 2018, **9**, 3400.
47 K.-N. Jung, J.-Y. Choi, H.-S. Shin, H. T. Huu, W. B. Im and J.-W. Lee, *Solid State Sci.*, 2020, **106**, 106334.
48 M. Li, X. Qiu, Y. Yin, T. Wei and Z. Dai, *J. Alloys Compd.*, 2023, **969**, 172406.
49 C. Zhao, Z. Yao, Q. Wang, H. Li, J. Wang, M. Liu, S. Ganapathy, Y. Lu, J. Cabana, B. Li, X. Bai, A. Aspuru-Guzik, M. Wagemaker, L. Chen and Y. S. Hu, *J. Am. Chem. Soc.*, 2020, **142**, 5742–5750.
50 Q. Zhou, L. Wang, W. Li, K. Zhao, M. Liu, Q. Wu, Y. Yang, G. He, I. P. Parkin, P. R. Shearing, D. J. L. Brett, J. Zhang and X. Sun, *Electrochem. Energy Rev.*, 2021, **4**, 793–823.
51 N. G. Garcia, J. M. Gonçalves, C. Real, B. Freitas, J. G. Ruiz-Montoya and H. Zanin, *Energy Storage Mater.*, 2024, **67**, 103213.
52 Z. C. Jian, J. X. Guo, Y. F. Liu, Y. F. Zhu, J. Wang and Y. Xiao, *Chem. Sci.*, 2024, **15**, 19698–19728.
53 Y. Gao, X. Zhang, H. Zhang, J. Peng, W. Hua, Y. Xiao, X. H. Liu, L. Li, Y. Qiao, J. Z. Wang, C. Zhang and S. Chou, *Adv. Mater.*, 2025, **37**, e2409782.
54 J. Peng, W. Zhang, Q. Liu, J. Wang, S. Chou, H. Liu and S. Dou, *Adv. Mater.*, 2022, **34**, 2108384.
55 X. Liu, Y. Cao and J. Sun, *Adv. Energy Mater.*, 2022, **12**, 2202532.
56 D. B. Miracle and O. N. Senkov, *Acta Mater.*, 2017, **122**, 448–511.
57 A. Amiri and R. Shahbazian-Yassar, *J. Mater. Chem. A*, 2023, **11**, 1512.
58 W. Zheng, G. Liang, Q. Liu, J. Li, J. A. Yuwono, S. Zhang, V. K. Peterson and Z. Guo, *Joule*, 2023, **7**, 2732–2748.
59 S. Yan, S. Luo, L. Yang, J. Feng, P. Li, Q. Wang, Y. Zhang and X. Liu, *J. Adv. Ceram.*, 2021, **11**, 158–171.
60 Y.-H. Tseng, Y.-C. Lin, Y.-H. Wu, J.-M. Ting and S.-H. Chung, *Energy Storage Mater.*, 2023, **68**, 107767.
61 Q. Wang, M. Zhao, H.-t. Yu, Y. Xie and T.-F. Yi, *Inorg. Chem. Front.*, 2024, **11**, 4249–4262.
62 X. L. Wang, E. M. Kim, T. G. Senthamaraikannan, D.-H. Lim and S. M. Jeong, *Chem. Eng. J.*, 2024, **484**, 149509.
63 Z. Wang, L. Fang, X. Fu, S. Zhang, H. Kong, H. Chen and F. Fu, *Chem. Eng. J.*, 2024, **480**, 148130.
64 H. Zhang, Y. Wang, J. Huang, W. Li, X. Zeng, A. Jia, H. Peng, X. Zhang and W. Yang, *Energy Environ. Mater.*, 2023, **7**, e12514.
65 S. Zhou, Y. Sun, T. Gao, J. Liao, S. Zhao and G. Cao, *Angew. Chem., Int. Ed.*, 2023, **62**, e202311930.
66 Y. Zhou, G. Xu, J. Lin, J. Zhu, J. Pan, G. Fang, S. Liang and X. Cao, *Nano Energy*, 2024, **128**, 109812.
67 A. Wetzel, M. von der Au, P. M. Dietrich, J. Radnik, O. Ozcan and J. Witt, *Appl. Surf. Sci.*, 2022, **601**, 154171.
68 H. Gao, J. Li, F. Zhang, C. Li, J. Xiao, X. Nie, G. Zhang, Y. Xiao, D. Zhang, X. Guo, Y. Wang, Y. M. Kang, G. Wang and H. Liu, *Adv. Energy Mater.*, 2024, **14**, 2304529.
69 Y. Ma, Y. Hu, Y. Pramudya, T. Diemant, Q. Wang, D. Goonetilleke, Y. Tang, B. Zhou, H. Hahn, W. Wenzel, M. Fichtner, Y. Ma, B. Breitung and T. Brezesinski, *Adv. Funct. Mater.*, 2022, **32**, 2202372.
70 Y. Zhang, Y. J. Zhou, J. P. Lin, G. L. Chen and P. K. Liaw, *Adv. Eng. Mater.*, 2008, **10**, 534–538.
71 Z. Zhou, Y. Ma, T. Brezesinski, B. Breitung, Y. Wu and Y. Ma, *Energy Environ. Sci.*, 2025, **18**, 19–52.
72 F. Li, Y. Zhao, L. Xia, Z. Yang, J. Wei and Z. Zhou, *J. Mater. Chem. A*, 2020, **8**, 12391–12397.
73 S. Akrami, P. Edalati, M. Fuji and K. Edalati, *Mater. Sci. Eng., R*, 2021, **146**, 100644.
74 R. Carroll, C. Lee, C. W. Tsai, J. W. Yeh, J. Antonaglia, B. A. Brinkman, M. LeBlanc, X. Xie, S. Chen, P. K. Liaw and K. A. Dahmen, *Sci. Rep.*, 2015, **5**, 16997.
75 M.-H. Tsai and J.-W. Yeh, *Mater. Res. Lett.*, 2014, **2**, 107–123.
76 R. Zhang, C. Wang, P. Zou, R. Lin, L. Ma, L. Yin, T. Li, W. Xu, H. Jia, Q. Li, S. Sainio, K. Kisslinger, S. E. Trask, S. N. Ehrlich, Y. Yang, A. M. Kiss, M. Ge, B. J. Polzin,

S. J. Lee, W. Xu, Y. Ren and H. L. Xin, *Nature*, 2022, **610**, 67–73.
77 A. Sarkar, Q. Wang, A. Schiele, M. R. Chellali, S. S. Bhattacharya, D. Wang, T. Brezesinski, H. Hahn, L. Velasco and B. Breitung, *Adv. Mater.*, 2019, **31**, e1806236.
78 W. Cheng, J. Liu, J. Hu, W. Peng, G. Niu, J. Li, Y. Cheng, X. Feng, L. Fang, M. S. Wang, S. A. T. Redfern, M. Tang, G. Wang and H. Gou, *Small*, 2023, **19**, e2301915.
79 G. Sun, H. Lin, S. Yao, Z. Wei, N. Chen, G. Chen, H. Zhao and F. Du, *Chem*, 2023, **29**, e202300413.
80 S. C. Kim, J. Wang, R. Xu, P. Zhang, Y. Chen, Z. Huang, Y. Yang, Z. Yu, S. T. Oyakhire, W. Zhang, L. C. Greenburg, M. S. Kim, D. T. Boyle, P. Sayavong, Y. Ye, J. Qin, Z. Bao and Y. Cui, *Nat. Energy*, 2023, **8**, 814–826.
81 X. Gao, X. Zhang, X. Liu, Y. Tian, Q. Cai, M. Jia and X. Yan, *Small Methods*, 2023, **7**, e2300152.
82 X. Liu, X.-Y. Liu, N. Zhang, P.-F. Wang, Z.-L. Liu, J.-H. Zhang, J. Shu, Y. Sun, C.-S. Li and T.-F. Yi, *Chem. Eng. J.*, 2024, **496**, 153743.
83 P. Hou, M. Gong, M. Dong, Z. Lin, J. Huang, H. Zhang and F. Li, *Energy Storage Mater.*, 2024, **72**, 103750.
84 B. L. Musicó, D. Gilbert, T. Z. Ward, K. Page, E. George, J. Yan, D. Mandrus and V. Keppens, *APL Mater.*, 2020, **8**, 040912.
85 S. J. McCormack and A. Navrotsky, *Acta Mater.*, 2021, **202**, 1–21.
86 X. Pu, H. Wang, T. Yuan, S. Cao, S. Liu, L. Xu, H. Yang, X. Ai, Z. Chen and Y. Cao, *Energy Storage Mater.*, 2019, **22**, 330–336.
87 M. Brahlek, M. Gazda, V. Keppens, A. R. Mazza, S. J. McCormack, A. Mielewczyk-Gryń, B. Musico, K. Page, C. M. Rost, S. B. Sinnott, C. Toher, T. Z. Ward and A. Yamamoto, *APL Mater.*, 2022, **10**, 110902.
88 A. Sarkar, B. Breitung and H. Hahn, *Scr. Mater.*, 2020, **187**, 43–48.
89 S. S. Aamlid, M. Oudah, J. Rottler and A. M. Hallas, *J. Am. Chem. Soc.*, 2023, **145**, 5991–6006.
90 Y. Chen, H. Fu, Y. Huang, L. Huang, X. Zheng, Y. Dai, Y. Huang and W. Luo, *ACS Mater. Lett.*, 2020, **3**, 160–170.
91 Y. Zeng, B. Ouyang, J. Liu, Y. W. Byeon, Z. Cai, L. J. Miara, Y. Wang and G. Ceder, *Science*, 2022, **378**, 1320–1324.
92 C. Zhao, F. Ding, Y. Lu, L. Chen and Y. S. Hu, *Angew. Chem., Int. Ed.*, 2020, **59**, 264–269.
93 K. Wang, W. Hua, X. Huang, D. Stenzel, J. Wang, Z. Ding, Y. Cui, Q. Wang, H. Ehrenberg, B. Breitung, C. Kubel and X. Mu, *Nat. Commun.*, 2023, **14**, 1487.
94 J.-W. Yeh, *Annales de Chimie Science des Matériaux*, 2006, **31**, 633–648.
95 Y. Ma, Y. Ma, S. L. Dreyer, Q. Wang, K. Wang, D. Goonetilleke, A. Omar, D. Mikhailova, H. Hahn, B. Breitung and T. Brezesinski, *Adv. Mater.*, 2021, **33**, 2101342.
96 W. Bao, H. Shen, Y. Zhang, C. Qian, G. Zeng, K. Jing, D. Cui, J. Xia, H. Liu, C. Guo, F. Yu, K. Sun and J. Li, *J. Mater. Chem. A*, 2024, **12**, 23179–23201.
97 L. Huang, J. Zhu, J.-X. Liu, H. Wu and G.-J. Zhang, *Chem. Eng. J.*, 2025, **507**, 160309.
98 B. Mortemard de Boisse, J. H. Cheng, D. Carlier, M. Guignard, C. J. Pan, S. Bordère, D. Filimonov, C. Drathen, E. Suard, B. J. Hwang, A. Wattiaux and C. Delmas, *J. Mater. Chem. A*, 2015, **3**, 10976–10989.
99 Y. F. Liu, K. Han, D. N. Peng, L. Y. Kong, Y. Su, H. W. Li, H. Y. Hu, J. Y. Li, H. R. Wang, Z. Q. Fu, Q. Ma, Y. F. Zhu, R. R. Tang, S. L. Chou, Y. Xiao and X. W. Wu, *Infomat*, 2023, **5**, e12422.
100 H. Guo, M. Avdeev, K. Sun, X. Ma, H. Wang, Y. Hu and D. Chen, *Chem. Eng. J.*, 2021, **412**, 128704.
101 S. Komaba, N. Yabuuchi, T. Nakayama, A. Ogata, T. Ishikawa and I. Nakai, *Inorg. Chem.*, 2012, **51**, 6211–6220.
102 K. Kubota, S. Kumakura, Y. Yoda, K. Kuroki and S. Komaba, *Adv. Energy Mater.*, 2018, **8**, 201703415.
103 Y. Li, X. Li, C. Du, H. Sun, Y. Zhang, Q. Liu, T. Yang, J. Zhao, C. Delmas, S. J. Harris, H. Chen, Q. Huang, Y. Tang, L. Zhang, T. Zhu and J. Huang, *ACS Energy Lett.*, 2021, **6**, 3960–3969.
104 Q. Shen, Y. Liu, L. Jiao, X. Qu and J. Chen, *Energy Storage Mater.*, 2021, **35**, 400–430.
105 L. Yu, H. Dong, Y.-X. Chang, Z. Cheng, K. Xu, Y.-H. Feng, D. Si, X. Zhu, M. Liu, B. Xiao, P.-F. Wang and S. Xu, *Sci. China: Chem.*, 2022, **65**, 2005–2014.
106 P. Zhou, Z. Che, J. Liu, J. Zhou, X. Wu, J. Weng, J. Zhao, H. Cao, J. Zhou and F. Cheng, *Energy Storage Mater.*, 2023, **57**, 618–627.
107 L. Yao, P. Zou, C. Wang, J. Jiang, L. Ma, S. Tan, K. A. Beyer, F. Xu, E. Hu and H. L. Xin, *Adv. Energy Mater.*, 2022, **12**, 2201989.
108 L.-Y. Li, M.-Y. Shen, J.-S. Wang, T. Wu and W.-C. Li, *ACS Appl. Mater. Interfaces*, 2025, **17**, 35631–35640.
109 F. Ding, C. Zhao, D. Xiao, X. Rong, H. Wang, Y. Li, Y. Yang, Y. Lu and Y.-S. Hu, *J. Am. Chem. Soc.*, 2022, **144**, 8286–8295.
110 X.-Y. Du, Y. Meng, H. Yuan and D. Xiao, *Energy Storage Mater.*, 2023, **56**, 132–140.
111 F. Fu, X. Liu, X. Fu, H. Chen, L. Huang, J. Fan, J. Le, Q. Wang, W. Yang, Y. Ren, K. Amine, S. G. Sun and G. L. Xu, *Nat. Commun.*, 2022, **13**, 2826.
112 X. Wang, Q. Kang, J. Sun, Z. Yang, Z. Bai, L. Yan, X. Meng, C. Wan and T. Ma, *J. Colloid Interface Sci.*, 2025, **691**, 137438.
113 Z. Liu, R. Liu, S. Xu, J. Tian, J. Li, H. Li, T. Yu, S. Chu, A. M. D'Angelo, W. K. Pang, L. Zhang, S. Guo and H. Zhou, *Angew. Chem., Int. Ed.*, 2024, **63**, e202405620.
114 Y. Xiao, H. R. Wang, H. Y. Hu, Y. F. Zhu, S. Li, J. Y. Li, X. W. Wu and S. L. Chou, *Adv. Mater.*, 2022, **34**, 2202695.
115 K. Walczak, A. Plewa, C. Ghica, W. Zając, A. Trenczek-Zając, M. Zając, J. Toboła and J. Molenda, *Energy Storage Mater.*, 2022, **47**, 500–514.
116 K. Tian, H. He, X. Li, D. Wang, Z. Wang, R. Zheng, H. Sun, Y. Liu, L. Du and Q. Wang, *J. Mater. Chem. A*, 2022, **10**, 14943–14953.
117 B. Wang, J. Ma, K. Wang, D. Wang, G. Xu, X. Wang, Z. Hu, C. W. Pao, J. L. Chen, L. Du, X. Du and G. Cui, *Adv. Energy Mater.*, 2024, **14**, 2401090.

118 F. Ding, P. Ji, Z. Han, X. Hou, Y. Yang, Z. Hu, Y. Niu, Y. Liu, J. Zhang, X. Rong, Y. Lu, H. Mao, D. Su, L. Chen and Y.-S. Hu, *Nat. Energy*, 2024, **9**, 1529–1539.
119 C.-C. Lin, H.-Y. Liu, J.-W. Kang, C.-C. Yang, C.-H. Li, H.-Y. T. Chen, S.-C. Huang, C.-S. Ni, Y.-C. Chuang, B.-H. Chen, C.-K. Chang and H.-Y. Chen, *Energy Storage Mater.*, 2022, **51**, 159–171.
120 J. Peng, W. Zhang, Q. Liu, J. Wang, S. Chou, H. Liu and S. Dou, *Adv. Mater.*, 2022, **34**, e2108384.
121 W. Wang, Y. Gang, Z. Hu, Z. Yan, W. Li, Y. Li, Q. F. Gu, Z. Wang, S. L. Chou, H. K. Liu and S. X. Dou, *Nat. Commun.*, 2020, **11**, 980.
122 A. Zhou, W. Cheng, W. Wang, Q. Zhao, J. Xie, W. Zhang, H. Gao, L. Xue and J. Li, *Adv. Energy Mater.*, 2020, **11**, 2000943.
123 Y. Huang, X. Zhang, L. Ji, L. Wang, B. B. Xu, M. W. Shahzad, Y. Tang, Y. Zhu, M. Yan, G. Sun and Y. Jiang, *Energy Storage Mater.*, 2023, **58**, 1–8.
124 J. Peng, B. Zhang, W. Hua, Y. Liang, W. Zhang, Y. Du, G. Peleckis, S. Indris, Q. Gu, Z. Cheng, J. Wang, H. Liu, S. Dou and S. Chou, *Angew. Chem., Int. Ed.*, 2023, **62**, e202215865.
125 B. Ran, R. Cheng, Y. Zhong, X. Zhang, T. Zhao, Z. Yang, C. Yang, J. Zhang and C. Fu, *Energy Storage Mater.*, 2024, **71**, 103583.
126 Y. He, S. L. Dreyer, Y. Y. Ting, Y. Ma, Y. Hu, D. Goonetilleke, Y. Tang, T. Diemant, B. Zhou, P. M. Kowalski, M. Fichtner, H. Hahn, J. Aghassi-Hagmann, T. Brezesinski, B. Breitung and Y. Ma, *Angew. Chem., Int. Ed.*, 2024, **136**, e202315371.
127 Y. Wang, N. Jiang, C. Yang, J. Liu, S. Sun, X. Wang, J. Yang and Y. Liu, *J. Mater. Chem. A*, 2024, **12**, 5170–5180.
128 Y. Zhang, J. Huang, L. Qiu, R. Jiao, Y. Zhang, G. Yang, L. Zhang, Z. Tian, E. Debroye, T. Liu, J.-F. Gohy, J. Hofkens and F. Lai, *ACS Appl. Mater. Interfaces*, 2024, **16**, 27684–27693.
129 X. H. Liu, W. H. Lai, J. Peng, Y. Gao, H. Zhang, Z. Yang, X. X. He, Z. Hu, L. Li, Y. Qiao, M. H. Wu and H. K. Liu, *Carbon Neutralization*, 2022, **1**, 49–58.
130 Y.-H. Chen, Y.-H. Zhao, S.-H. Tian, P.-F. Wang, F. Qiu and T.-F. Yi, *Composites, Part B*, 2023, **266**, 111030.
131 L. Sharma, S. P. Adiga, H. N. Alshareef and P. Barpanda, *Adv. Energy Mater.*, 2020, **10**, 2001449.
132 X. Ge, H. Li, J. Li, C. Guan, X. Wang, L. He, S. Li, Y. Lai and Z. Zhang, *Small*, 2023, **19**, 2302609.
133 G. Li, Y. Cao, J. Chen, K. Zhang, Y. Liu, X. Zhang, Y. Wang, F. Wang and Y. Xia, *Small Methods*, 2024, **8**, 2301745.
134 N. Jiang, X. Wang, H. Zhou, Y. Wang, S. Sun, C. Yang and Y. Liu, *Small*, 2024, **20**, e2308681.
135 N. Zhang, X. Dong, Q. Yan, J. Wang, F. Jin, J. Liu, D. Wang, H. Liu, B. Wang and S. Dou, *Energy Storage Mater.*, 2024, **72**, 103734.
136 X. Chen, K. Chen, F. Ji, L. Han, X. Ai, Y. Cao and Y. Fang, *Adv. Energy Mater.*, 2025, **15**, 2500502.
137 M. Du, K. Li, N. Yu, Z. L. Hao, J. Z. Guo, H. J. Liang, Z. Y. Gu, X. H. Zhang, K. Y. Zhang, Y. Liu, J. L. Yang, Y. T. Liu and X. L. Wu, *Adv. Mater.*, 2025, **37**, 2418219.
138 P. Dong, F. Peng, Q. Zhang, H. Wang, Y. Chu, C. Chen and C. Yang, *Angew. Chem., Int. Ed.*, 2025, **64**, e202502693.
139 W. Zhang, L. He, J. Li, R. Yu, Z. Xu, Y. Wu, H. Qu, Q. Zhang, J. Li, X. Wu, Q. Fu, Y. Lai, G. Zhou, G. He and I. P. Parkin, *Energy Environ. Sci.*, 2025, **18**, 7278–7290.
140 S. Schweidler, M. Botros, F. Strauss, Q. Wang, Y. Ma, L. Velasco, G. Cadilha Marques, A. Sarkar, C. Kübel, H. Hahn, J. Aghassi-Hagmann, T. Brezesinski and B. Breitung, *Nat. Rev. Mater.*, 2024, **9**, 266–281.
141 T. Zhang, J. Kong, C. Shen, S. Cui, Z. Lin, Y. Deng, M. Song, L. Jiao, H. Huang, T. Jin and K. Xie, *ACS Energy Lett.*, 2023, **8**, 4753–4761.
142 Q. Liu, W. Zheng, G. Liu, J. Hu, X. Zhang, N. Han, Z. Wang, J. Luo, J. Fransaer and Z. Lu, *ACS Appl. Mater. Interfaces*, 2023, **15**, 9324–9330.
143 Z. Chen, Y. Deng, J. Kong, W. Fu, C. Liu, T. Jin and L. Jiao, *Adv. Mater.*, 2024, **36**, e2402008.
144 Q. Liu, W. Zheng, X. Su, X. Zhang, N. Han, Z. Wang, J. Luo, Z. Lu and J. Fransaer, *Chem. Eng. J.*, 2023, **452**, 139337.
145 M. Widom, *J. Mater. Res.*, 2018, **33**, 2881–2898.
146 J. M. Rickman, H. M. Chan, M. P. Harmer, J. A. Smeltzer, C. J. Marvel, A. Roy and G. Balasubramanian, *Nat. Commun.*, 2019, **10**, 2618.
147 T. A. A. Batchelor, J. K. Pedersen, S. H. Winther, I. E. Castelli, K. W. Jacobsen and J. Rossmeisl, *Joule*, 2019, **3**, 834–845.
148 V. Sorkin, Z. G. Yu, S. Chen, T. L. Tan, Z. H. Aitken and Y. W. Zhang, *Sci. Rep.*, 2022, **12**, 11894.
149 Y. Yao, Z. Liu, P. Xie, Z. Huang, T. Li, D. Morris, Z. Finfrock, J. Zhou, M. Jiao, J. Gao, Y. Mao, J. J. Miao, P. Zhang, R. Shahbazian-Yassar, C. Wang, G. Wang and L. Hu, *Sci. Adv.*, 2020, **6**, eaaz0510.
150 K. Kaufmann, D. Maryanovsky, W. M. Mellor, C. Zhu, A. S. Rosengarten, T. J. Harrington, C. Oses, C. Toher, S. Curtarolo and K. S. Vecchio, *npj Comput. Mater.*, 2020, **6**, 42.
151 R. Machaka, *Comput. Mater. Sci.*, 2021, **188**, 110244.
152 Z. Pei, J. Yin, J. A. Hawk, D. E. Alman and M. C. Gao, *npj Comput. Mater.*, 2020, **6**, 50.
153 W. Huang, P. Martin and H. L. Zhuang, *Acta Mater.*, 2019, **169**, 225–236.
154 Y. Zhang, C. Wen, C. Wang, S. Antonov, D. Xue, Y. Bai and Y. Su, *Acta Mater.*, 2020, **185**, 528–539.
155 D. Dai, T. Xu, X. Wei, G. Ding, Y. Xu, J. Zhang and H. Zhang, *Comput. Mater. Sci.*, 2020, **175**, 42.
156 A. van de Walle and M. Asta, *MRS Bull.*, 2019, **44**, 252–256.
157 M. Kumbhakar, A. Khandelwal, S. K. Jha, M. V. Kante, P. Keßler, U. Lemmer, H. Hahn, J. Aghassi-Hagmann, A. Colsmann, B. Breitung, L. Velasco and S. Schweidler, *Adv. Energy Mater.*, 2023, **13**, 202204337.
158 M. Moorehead, K. Bertsch, M. Niezgoda, C. Parkin, M. Elbakhshwan, K. Sridharan, C. Zhang, D. Thoma and A. Couet, *Mater. Des.*, 2020, **187**, 108358.
159 Z. Rao, P. Y. Tung, R. Xie, Y. Wei, H. Zhang, A. Ferrari, T. P. C. Klaver, F. Kormann, P. T. Sukumar, A. Kwiatkowski da Silva, Y. Chen, Z. Li, D. Ponge,

J. Neugebauer, O. Gutfleisch, S. Bauer and D. Raabe, *Science*, 2022, **378**, 78–85.

160 K. Kaufmann and K. S. Vecchio, *Acta Mater.*, 2020, **198**, 178–222.

161 Y. Bi, J. Tao, Y. Wu, L. Li, Y. Xu, E. Hu, B. Wu, J. Hu, C. Wang, J. G. Zhang, Y. Qi and J. Xiao, *Science*, 2020, **370**, 1313–1317.

162 S. Yin, W. Deng, J. Chen, X. Gao, G. Zou, H. Hou and X. Ji, *Nano Energy*, 2021, **83**, 105854.

163 C. Zuo, Z. Hu, R. Qi, J. Liu, Z. Li, J. Lu, C. Dong, K. Yang, W. Huang, C. Chen, Z. Song, S. Song, Y. Yu, J. Zheng and F. Pan, *Adv. Energy Mater.*, 2020, **10**, 2000363.

164 G. Liang, V. K. Peterson, Z. Wu, S. Zhang, J. Hao, C. Z. Lu, C. H. Chuang, J. F. Lee, J. Liu, G. Leniec, S. M. Kaczmarek, A. M. D'Angelo, B. Johannessen, L. Thomsen, W. K. Pang and Z. Guo, *Adv. Mater.*, 2021, **33**, e2101413.

165 S. D. Zhang, M. Y. Qi, S. J. Guo, Y. G. Sun, X. X. Tan, P. Z. Ma, J. Y. Li, R. Z. Yuan, A. M. Cao and L. J. Wan, *Small Methods*, 2022, **6**, e2200148.